Title

Skeletal muscle TFEB signaling promotes central nervous system function and reduces neuroinflammation during aging and neurodegenerative disease.

Journal

Cell Reports, 42(11)

Authors

Matthews, Ian
Birnbaum, Allison
Gromova, Anastasia
et al.

Publication Date

2023-11-28

DOI

10.1016/j.celrep.2023.113436

Peer reviewed

HHS Public Access

Author manuscript

Cell Rep. Author manuscript; available in PMC 2024 February 05.

Published in final edited form as:

Cell Rep. 2023 November 28; 42(11): 113436. doi:10.1016/j.celrep.2023.113436.

Skeletal muscle TFEB signaling promotes central nervous system function and reduces neuroinflammation during aging and neurodegenerative disease

Ian Matthews[1], **Allison Birnbaum**[1], **Anastasia Gromova**[2], **Amy W. Huang**[1], **Kailin Liu**[1], **Eleanor A. Liu**[1], **Kristen Coutinho**[4], **Megan McGraw**[5], **Dalton C. Patterson**[5], **Macy T. Banks**[5], **Amber C. Nobles**[6], **Nhat Nguyen**[2], **Gennifer E. Merrihew**[7], **Lu Wang**[8], **Eric Baeuerle**[9,10,11], **Elizabeth Fernandez**[9,10,11], **Nicolas Musi**[12], **Michael J. MacCoss**[7], **Helen C. Miranda**[13,14,15], **Albert R. La Spada**[2,3,*], **Constanza J. Cortes**[1,16,*]

[1]Leonard Davis School of Gerontology, University of Southern California, Los Angeles, CA 90007, USA

[2]Department of Pathology and Laboratory Medicine, UCI Institute for Neurotherapeutics, University of California, Irvine, Irvine, CA 92697, USA

[3]Department of Neurology and Department of Biological Chemistry, UCI Institute for Neurotherapeutics, University of California, Irvine, Irvine, CA 92697, USA

[4]Comprehensive Diabetes Center, University of Alabama at Birmingham, Birmingham, AL 35294, USA

[5]Department of Cell, Developmental and Integrative Biology, University of Alabama at Birmingham, Birmingham, AL 35294, USA

[6]Department of Neurology, University of Alabama at Birmingham, Birmingham, AL 35294, USA

[7]Department of Genome Sciences, University of Washington, Seattle, WA 98195, USA

[8]Department of Environmental and Occupational Health Sciences, University of Washington, Seattle, WA 98195, USA

[9]Department of Pharmacology, University of Texas Health San Antonio, San Antonio, TX 78229, USA

[10]Barshop Institute for Longevity and Aging Studies, University of Texas Health San Antonio, San Antonio, TX 78229, USA

*Correspondence: alaspada@uci.edu (A.R.L.S.), cjc_149@usc.edu (C.J.C.).

AUTHOR CONTRIBUTIONS

I.M., C.J.C., A.G., H.C.M., A.B., A.W.H., K.L., E.A.L., K.C., M.M., D.C.P., M.T.B., A.C.N., N.N., G.E.M., L.W., M.J.M., N.M., E.B., and E.F. performed the experimental work and reviewed and edited the manuscript. C.J.C. and I.M. wrote and edited the manuscript. C.J.C. and A.R.L.S. conceptualized the experiments outlined here and obtained all associated funding.

DECLARATION OF INTERESTS

The authors declare no competing interests.

SUPPLEMENTAL INFORMATION

Supplemental information can be found online at https://doi.org/10.1016/j.celrep.2023.113436.

[11]Geriatric Research, Education and Clinical Center, South Texas Veterans Health Care Network, San Antonio, TX 78229, USA

[12]Department of Medicine, Cedars-Sinai Medical Center, Los Angeles, CA 90048, USA

[13]Department of Genetics and Genome Sciences, School of Medicine, Case Western Reserve University, Cleveland, OH 44106, USA

[14]Department of Neurosciences, School of Medicine, Case Western Reserve University, Cleveland, OH 44106, USA

[15]RNA Center, School of Medicine, Case Western Reserve University, Cleveland, OH 44106, USA

[16]Lead contact

SUMMARY

Skeletal muscle has recently arisen as a regulator of central nervous system (CNS) function and aging, secreting bioactive molecules known as myokines with metabolism-modifying functions in targeted tissues, including the CNS. Here, we report the generation of a transgenic mouse with enhanced skeletal muscle lysosomal and mitochondrial function via targeted overexpression of transcription factor E-B (TFEB). We discovered that the resulting geroprotective effects in skeletal muscle reduce neuroinflammation and the accumulation of tau-associated pathological hallmarks in a mouse model of tauopathy. Muscle-specific TFEB overexpression significantly ameliorates proteotoxicity, reduces neuroinflammation, and promotes transcriptional remodeling of the aged CNS, preserving cognition and memory in aged mice. Our results implicate the maintenance of skeletal muscle function throughout aging in direct regulation of CNS health and disease and suggest that skeletal muscle originating factors may act as therapeutic targets against age-associated neurodegenerative disorders.

Graphical Abstract

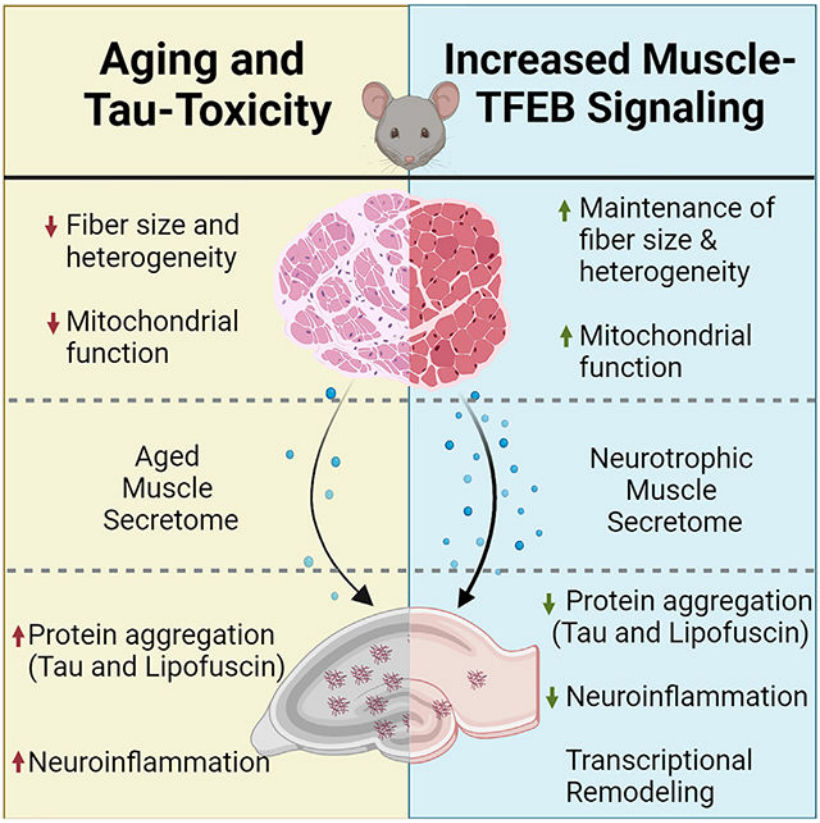

In brief

Matthews et al. demonstrate that activation of the muscle-to-brain axis *in vivo* promotes robust neuroprotective effects during aging and neurodegenerative disease. These benefits are associated with transcriptional remodeling of the hippocampus and sex-biased modulation of classical pathways known to decline with age, including synaptic plasticity, mitochondrial function, and ribosomal metabolism.

INTRODUCTION

Aging is associated with an organism-wide progressive loss of tissue form and function, broadly characterized by the "hallmarks of aging."[1] In particular, the aging central nervous system (CNS)[1,2] exhibits a global loss in protein homeostasis (proteostasis), impaired neuroplasticity/resilience, and an increase in neuroinflammation.[2,3] These alterations are believed to render the aging CNS vulnerable to age-associated dysfunction and the development of neurodegeneration.[2]

Over the last decade, growing evidence has suggested that the periphery contributes to the etiology of age-associated neurodegenerative diseases.[4–8] Manipulation of skeletal muscle protein quality control pathways protects against the accumulation of aggregation-prone disease proteins in the invertebrate brain/retina.[5,8,9] The mechanisms responsible for these benefits remain poorly understood, some of these effects are mediated by secreted factors that communicate metabolic and inflammatory signals between tissues.[5,7,9]

Blood circulating factors have recently arisen as potent regulators of mammalian CNS aging and metabolism.[10–13] Exposure to young plasma can rescue function in the aging CNS[12–14] by decreasing neuroinflammation[15] and enhancing neurogenesis.[10] Increasing the levels of these individual factors in peripheral circulation is sufficient to rejuvenate the aged CNS,[12,16,17] supporting the existence of geroprotective circulating factors with CNS-targeting effects. Although the source and identity of these neuroprotective circulating cytokines are unclear, several are known to be secreted from skeletal muscle,[5,18–20] an unconventional endocrine organ that secretes a myriad of bioactive factors that induce metabolic changes in distant tissues such as liver,[21] adipose,[22] and the CNS.[19]

This muscle-to-brain signaling axis may have important implications for CNS aging and age-associated neurodegenerative disease.[19,23,24] Skeletal muscle function is a predictor for phenotypic and clinical outcomes in age-associated neurodegenerative diseases, including Alzheimer's disease (AD) and Parkinson's disease (PD).[25,26] We have shown that disruption of skeletal muscle autophagy initiates the pathogenic cascade culminating in motor-neuron toxicity and death in the polyglutamine disease spinal and bulbar muscular atrophy.[27] Rescuing proteotoxicity specifically in skeletal muscle was sufficient to rescue motor-neuron degeneration and extend lifespan in this model, despite robust misfolded protein burden in the brain.[28] We then demonstrated the feasibility of delivering antisense oligonucleotides peripherally in reducing skeletal muscle misfolded protein expression and rescuing neurological phenotypes,[29] confirming that therapeutic targeting of skeletal muscle can benefit the CNS.

Skeletal muscle metabolism is regulated in part by transcription factor E-B (TFEB), a master regulator of the lysosomal-to-nucleus signaling that integrates cellular metabolism and lysosomal function.[30–32] TFEB expression and function are strongly induced in skeletal muscle in response to interventions with neuroprotective effects against aging and neurodegenerative disease, including low nutrient conditions[33,34] and exercise.[35,36] TFEB controls muscle metabolic flexibility during exercise, inducing the expression of genes involved in mitochondrial biogenesis, fatty acid oxidation, and oxidative phosphorylation.[36] However, the precise role of TFEB-dependent signaling in skeletal muscle during aging and its impact on the muscle-to-brain axis remains largely unknown.

Here, we report the generation of a transgenic mouse with enhanced muscle metabolism via lifelong overexpression of TFEB. The resulting enhanced TFEB signaling protects against the onset of age-associated mitochondrial dysfunction in aging skeletal muscle. Overexpression of TFEB in skeletal muscle significantly reduces hippocampal accumulation of neuropatho-logical hallmarks and reduces neuroinflammation in a mouse model of tauopathy, despite no exogenous activation of the transgene in the CNS. Muscle TFEB overexpression ameliorates proteotoxicity, reduces neuroinflammation, and promotes transcriptional remodeling of the "healthy" aged CNS, preserving cognitive performance in aging mice. Our results implicate maintenance of skeletal muscle function in regulating mammalian CNS health, and suggest that skeletal muscle-originating factors may act as therapeutic targets against age-associated neurodegenerative diseases.

RESULTS

TFEB overexpression maintains fiber type composition, function, and metabolism-associated networks in aging skeletal muscle

We derived a line of conditional transgenic mice carrying the β-actin promoter in combination with the CMV enhancer (CAGGS) and with a floxed 3x-FLAG-eGFP STOP cassette placed 5′ to a 3x-FLAG-human *TFEB* transgene (i.e., fxSTOP-TFEB transgenic mice) (Figure 1A). In the presence of Cre-recombinase, the STOP codon cassette will be excised, allowing expression of the human TFEB transgene, also known as a Cre-*loxP* ON system. To overexpress TFEB specifically in skeletal muscle, we crossed fxSTOP-TFEB mice with human skeletal actin (HSA)-Cre mice to achieve widespread expression of Cre-recombinase in myogenic cells.[37]

The resulting cTFEB;HSACre mice of both sexes exhibit a strong induction of human *TFEB* mRNA expression in skeletal muscle tissue (Figure S1A, quadriceps), which is still prominent at age 24 months (Figure S1B, quadriceps), suggesting that overexpression of the transgene remains active even at very old age. Immunoblotting of quadriceps confirmed robust expression of 3x-FLAG-TFEB protein in cTFEB;HSACre muscle lysates of both sexes in young and aged muscle (Figure 1B), with TFEB protein levels ~2-fold higher in male vs. female cTFEB;HSACre mice at both ages examined. We confirmed nuclear localization of human TFEB in cTFEB;HSACre skeletal muscle myonuclei via immunofluorescence (Figure S1C).

Next, we confirmed skeletal muscle-only overexpression of TFEB protein in cTFEB;HSACre mice by immunoblotting for the presence of the biologically inert 3x-FLAG-eGFP cassette upstream of the STOP codon (Figure 1A) and no exogenous expression of 3x-FLAG-TFEB in other highly metabolic non-myogenic tissues, including brown adipose tissue (Figure S1D) and liver (Figure S1E). We detected mild expression of human *TFEB* mRNA levels in cTFEB;HSACre hearts, confirming low-level crossover into cardiac tissue in the HSACre model. However, this cardiac expression was ~400-fold less in young animals and ~15-fold less in aged animals than levels detected in skeletal muscle at the same ages (Figure S1A, ventricles). Importantly, we could not detect 3x-FLAG-TFEB protein via immunoblotting in cTFEB;HSACre ventricle protein lysates (Figure S1F). This suggests that, despite some HSACre “leakiness” into cardiac muscle, synthesis of exogenous TFEB protein in heart tissue is below detectable levels, confirming the high skeletal muscle tropism of HSACre-driven expression. We did not detect expression of exogenous human TFEB mRNA or protein in the hippocampus (Figures S1A and S1B, hippocampus) or hemibrain protein lysates (Figure S1G). To further confirm no CNS expression of transgenes in the HSACre line, we directly assessed the Cre-mediated recombination of an additional transgene reporter in TdTomato Ai9;HSACre mice. Consistent with our cTFEB;HSACre results, we confirmed robust tdTomato fluorescence in skeletal muscle (Figure S1H) but no detectable fluorescence in the CNS (Figure S1I), including the hippocampus (Figure S1I, insets), of TdTomato Ai9;HSACre mice. Overall, these data confirm previous reports of striated muscle-specific Cre-mediated recombination using the HSACre line,[37] and establish

our cTFEB;HSACre mice as an effective model to generate spatiotemporally controlled transgenic expression of human TFEB only in skeletal muscle.

Analysis of skeletal muscle wet weight, a proxy for muscle size, confirmed 20%–30% of quadriceps muscle weight is lost during aging (6–8 to 22–24 months of age) in our control animals (Figures 1C and 1D). Interestingly, while cTFEB;HSACre muscle wet weight trended toward larger muscle weights in young cTFEB;HSACre animals without reaching significance, there was a robust preservation of quadriceps and gastrocnemius skeletal muscle mass in aged (22–24 months old) transgenic mice of both sexes (Figures 1C and 1D), without any changes in total body weight at either age examined (Figure 1E). Overexpression of TFEB significantly decreases the number of small fibers (<1,500 μm^2) and increases the number of large fibers (>1,500 μm^2) in young gastrocnemius skeletal muscle of both sexes (Figures 1F and 1G), accompanied by an increase in abundance of type 1 (~1% more) and type 2A (~9% more) fibers (Figures 1H–1K) and an increase in the cross-sectional area of type 2B (~200 μm^2 larger) and 2× (~300 μm^2 larger) fibers with no changes in Feret's minimum diameter (Figures S2A–S2H), which was prevalent in male mice and trending in female mice. While aged control male gastrocnemius muscle lost a significant portion of large fibers, they were not altered in aged male cTFEB;HSACre muscle (Figures 1F and 1G). Abundance of type 1 and type 2A fibers was still prevalent in aged male cTFEB;HSA-Cre muscle (Figures 1H–1K), suggesting that TFEB overexpression remodels both fast-twitch glycolytic and oxidative fiber fibers and that these changes are maintained during aging. We also determined that, at age 6 months, muscle-TFEB-overexpressing mice had a 20% (males) and 40% (females) longer maximum running distance to exhaustion (Figure 1L) and engaged in more total work (Figure 1M) than their control littermates. This enhanced physical performance was still present in aged female cTFEB;HSACre transgenic mice (Figure 1M). These results suggest that lifelong expression of TFEB prevents fiber type atrophy and alters fiber type switching in aging skeletal muscle, ultimately preserving muscle size and running performance during aging.

Given the principal role of TFEB-regulated signaling (such as autophagy/lysosomal function) on muscle health,[38,39] and the profound geroprotective effects of TFEB overexpression on muscle fiber types, muscle size, and exercise performance in aging muscle (Figure 1), we examined the overall changes in the skeletal muscle proteome in response to TFEB overexpression throughout aging. Proteome profiling revealed differential abundance of 909 proteins associated with TFEB overexpression in young (6 months old) skeletal muscle (Figure 2A). Of these, 857 (~94%) were significantly overrepresented and 52 (~6%) were underrepresented compared with controls. At age 18 months, a time point where age-associated dysfunction is prevalent in murine skeletal muscle,[40] we identified 351 differentially expressed proteins in TFEB-expressing skeletal muscle (Figure 2B). Of these, 283 proteins (~81%) were significantly enriched and 68 proteins (~19%) were significantly decreased in cTFEB;HSACre muscle, with only 53 of these proteins being uniquely expressed in older mice. Importantly, at both ages examined, TFEB remained significantly overexpressed (Figures 2A and 2B, boxes), confirming that exogenous muscle TFEB expression is maintained across the lifespan of cTFEB;HSACre mice (Figure 1B).

To visualize the networks of differentially expressed proteins associated with TFEB overexpression, we performed a functional enrichment analysis on all overexpressed proteins using the STRING protein-protein interaction network[41] (Figure 2C). Using TFEB as "bait" for functional connectivity nodes, we identified two clear interaction networks: the first associated with lysosomal biogenesis and function (Figure 2C, blue), and included Lamp1 (an essential lysosomal structural protein), Grn (progranulin), and Psap (prosaposin), as well as the lysosomal proteases Ctsb (cathepsin B), Ctsd (cathepsin D), and cathepsin L. The second interaction network was associated with central muscle proteostasis and metabolic signaling pathways including mTOR, Akt, and GSK3β (Figure 2C, green). Both of these nodes are key elements of the signaling network controlled by TFEB-mediated transcription,[31,32] were previously reported to be transcriptionally elevated in skeletal muscle after acute TFEB overexpression,[36] and are central regulators of aging.[1] KEGG enrichment analysis revealed that central proteostasis categories were significantly upregulated in young TFEB-overexpressing skeletal muscle, including hypoxia-inducible factor 1 (HIF-1) signaling, proteasome, and autophagy/lysosomal function categories (Figure 2D, orange). Importantly, this enrichment in proteostasis categories and TFEB-regulated nodes of signaling was also present in our aging cohorts (Figure 2D, top).
We confirmed functional activation of TFEB-dependent transcription in cTFEB;HSACre muscle, using our previously reported TFEB-responsive muscle gene targets,[27] including *Lamp1*, *Atg5* (a key regulator of autophagy initiation), *Ctsd*, and *Ctsb* (Figure 2E). Immunoblotting studies confirmed significant increases in Lamp1 and Ctsd protein in cTFEB;HSA-Cre muscle (Figure 2F). Consistent with previous studies,[30,34,42] we detected significant increases in the number of LAMP1+ puncta and total LAMP1+ area in cross-sections of young female (and similar trends in male) cTFEB;HSACre muscle (Figure 2G), with no changes to LC3II/LCI ratios or total polyubiquitinated protein levels in cTFEB;HSACre mice (Figure S2I). These findings confirm physiologically significant increases in TFEB-dependent transcription[36] and lysosomal biogenesis[32,36] in cTFEB;HSACre skeletal muscle.

Additional functional categories enriched in our proteomics analysis related to cellular metabolism and mitochondrial function, including thermogenesis, oxidative phosphorylation, and pyruvate metabolism (Figure 2D, gold). We also detected central fatty acid metabolism pathways, including PPAR signaling and metabolism, and degradation and biosynthesis of fatty acids (Figure 2D, green). This is consistent with how acute TFEB expression in young skeletal muscle induces the expression of genes involved in mitochondrial biogenesis and oxidative phosphorylation.[36] We confirm that these changes in cTFEB;HSACre muscle are maintained throughout aging, particularly those associated with mitochondrial metabolism and fatty acid metabolism (Figure 2D, top, gold and green). KEGG analysis showed enrichment in cTFEB;HSACre muscle for classical age-associated signaling pathways, including insulin-IGF1 signaling and AMPK signaling[1] (Figure 2D, blue). We also detected multiple hits for amino acid metabolism pathways, such as catabolism of branched chain amino acids, including valine, leucine. and isoleucine metabolism (Figure 2D, purple). Importantly, these changes were still evident in our aged cohorts (Figure 2D, top). We next directly assessed mitochondrial function using high-resolution respirometry with simultaneous measurements ROS production assays.[43]

As reported previously for soleus skeletal muscle,[43] oxygen consumption rates decrease with aging across all mitochondrial complexes in semi-permeabilized soleus muscle of control mice of both sexes (age 6 vs. 18 months) (Figures 2H and 2I). Whereas there was no difference in mitochondrial respiration rates between control and TFEB-overexpressing skeletal muscle at young ages, respiration rates of aged cTFEB;HSACre muscle remained comparable with their young counterparts across all complexes examined (Figure 2H and 2I), particularly in female muscle. Together with increased exercise capacity in cTFEB;HSACre mice (Figures 1L and 1M), this suggests that muscle-TFEB overexpression promotes maintenance of mitochondrial function and bioenergetic reserves, preventing the age-associated decline of mitochondrial respiration in skeletal muscle.[1,43]

The skeletal muscle “secretome” is highly dynamic, responding to physiological and pathophysiological stimuli[44,45] and potentially changing with age.[45] We pursued additional *in silico* analysis on our proteomics cohorts to identify unique age- and genotype-associated signatures of potentially secreted proteins through the Vertebrate Secretome Database,[46] and identified multiple proteins with predicted secreted profiles to be differentially expressed in young and aged TFEB-expressing muscle (Figure 3A). Some secreted proteins exhibited upregulation (e.g., nucleobindin-1, angiopoietin-related protein 1) or downregulation (collagen alpha-1 (I) chain), only in young cTFEB;HSA-Cre muscle (Figure 3A, green). Others remained upregulated at both ages (prosaposin, mammalian ependymin-related protein 1 [MERP1], and dehydrogenase/reductase SDR family member 7C [D/R SDR7C]) (Figure 3A, overlap), or were only differentially expressed in aged muscle (biglycan-1 [PG-S1], Figure 3A, blue). Ctsb, a previously documented muscle-originating secreted factor with known CNS-targeting effects[20] and a known target of TFEB-dependent transcription (Figure 2E)[32] was our top upregulated hit at both ages examined. We validated significant increases in pro-enzyme levels of Ctsb in both sexes and at both ages examined (Figure 3B), and significant increases in mature (secreted) Ctsb isoforms in aged cTFEB;HSACre muscle (Figure 3B). We detected trends toward increased levels of circulating Ctsb in the serum of female cTFEB;HSACre mice (Figure 3E). Given the potent remodeling of the lysosomal network associated with activation of TFEB-mediated transcription (Figure 2),[30–32] our data suggest that overexpression of TFEB in skeletal muscle drives increased expression and secretion of mature Ctsb, a CNS targeting factor, into circulation.

Enhanced skeletal muscle TFEB signaling reduces accumulation of hyperphosphorylated tau and microglial activation in a mouse model of tau pathology

To assess the neuroprotective effects of enhanced muscle-TFEB on age-associated neurodegenerative disease, we derived cTFEB;HSACre mice in the MAPT P301S (PS19) background, a well-known model of neurofibrillary tangle toxicity and tauopathies.[47] This model is characterized by prominent accumulation of hyperphosphorylated mutant human MAPT protein and pronounced neuroinflammation, including microgliosis and astrocyte reactivity in the hippocampus.[47]

We confirmed muscle-restricted 3x-FLAG-TFEB overexpression in muscle lysates from MAPT P301S;cTFEB;HSACre mice, and the presence of human MAPT/tau protein in hippocampal lysates of both groups via immunoblotting (Figure 4A). As reported

previously,[47] at 9 months of age there is robust accumulation of Ser202/Thr205 hyperphosphorylated tau in the hippocampal dentate gyrus of MAPT P301S mice[47] (Figure 4B, middle panel). Conversely, we noted a significant reduction in the total fluorescence counts of AT8-positive phosphorylated tau in the dentate gyrus of MAPT P301S;cTFEB;HSACre mice (Figure 4B, purple) compared with MAPT P301S littermates (Figure 4B, teal). This reduction was particularly evident in the levels of "intracellular tau" (Figure 4B, insets), suggesting reduced accumulation of toxic tau species[48] in the hippocampus of MAPT P301S; cTFEB;HSACre mice. We confirmed similar but less-striking reductions in Thr231 phospho-tau (another primary site of tau phosphorylation) immunostaining (Figure S3A), suggesting overall tau hyperphosphorylation reductions in the hippocampus of MAPT P301S transgenic mice with TFEB overexpression in skeletal muscle.

Astrocytes and microglia are key mediators of neuroinflammation, and undergo morphological/functional alterations during neurodegenerative disease, including changes in ramification and cellular process complexity[49] and increased reactivity phenotypes.[50] We confirmed significant increases in the staining for GFAP+ structures (a marker of astrocyte reactivity) in the dentate gyrus of 9-month-old MAPT P301S mice (Figure 4C, teal) compared with their MAPT-negative littermate controls (Figure 4C, gold). We detected significant increases in the volume of IBA1+ microglia in the same brain region (Figure 4C, teal), consistent with previous reports in the MAPT P301S model indicating high levels of neuroinflammation.[47,51] Strikingly, we noted significant reductions in both of these pro-inflammatory glial morphometric parameters in the hippocampus of MAPT P301S;cTFEB;HSACre littermates (Figure 4C, purple), suggesting overall reduced hippocampal neuroinflammation during symptomatic disease stages through activation of skeletal muscle TFEB expression.

Enhanced muscle TFEB expression promotes neurotrophic signaling and reduces hippocampal neuroinflammation in MAPT P301S transgenic mice

To gain more precise insights into disease-relevant transcriptional changes in the hippocampus of MAPT P301S mice with enhanced muscle-TFEB expression, we assessed the expression of targeted genes curated from human and pre-clinical models of AD that robustly capture disease-relevant signatures and their modifications after pre-clinical interventions.[52] Of 770 genes in the NanoString nCounter Mouse Alzheimer's Disease Panel, there were 24 individual differentially expressed genes in MAPT P301S;cTFEB;HSACre hippocampi compared with MAPT P301S+ between both sexes (Figures S3B and S3C). Most differentially regulated genes were downregulated (18 of 24), consistent with their identity as transcriptional drivers of disease,[52] and were associated with microglial activation (*Rhoc*, *Clic1*), neuronal function (*Gdap1l1*, *Amot*, *Map3k9*), phospholipid and cholesterol remodeling (*Ano6*, *Cyp27a1*), growth factor signaling (*Vgf*), endothelial cell migration/matrix adhesion (*Rras*, *Cdc42Ep1*), and guanine nucleotide exchange factors (*Dock3*). Multiple downregulated genes were associated with novel variants and loci associated with phosphorylated-tau and $A\beta_{1-40}$ levels in the human temporal cortex (*Pbxip1*[53]), increased polygenic neurodegenerative disease risk (*Prkd3*, *Arhgap31*), and predictors of the rate of cognitive decline in AD (*Hecw1*[54]). Additional

transcriptional changes of significance include genes of unknown function but classified as transcriptional identifiers of AD progression (*Ptprn*, *Cpne2*, and *Eri2*).[52] Upregulated transcripts included gene repressors (*Zbtb33*), modulators of neuroinflammation (*Pecam1*), and neurodegeneration (*Scna*), as well as a carbohydrate transmembrane transporter (*Tmem144*) and a GTPase nucleotide exchange factor (*Rcc1*).

Annotation of differentially co-expressed/co-functional clusters revealed significant reductions in the microglial activation module (composed of 63 genes associated with microglial activation during AD progression) (Figure 4D) in the hippocampi of 6-month-old female (but not male) MAPT P301S;cTFEB;HSACre mice compared with MAPT P301S littermates. This is consistent with reduced neuroinflammation in MAPT P301S;cTFEB;HSA-Cre hippocampi, measured via glial morphometric analysis (Figure 4C). We also detected a sex bias in the trophic factor functional cluster (composed of genes *Arhgdib*, *Bcl2*, *Calm3*, *Camk4*, *Gab1*, *Mapk9*, *Mapkapk2*, *Ntrk2*, *Pik3r1*, and *Psen1*), with a significant improvement back to baseline expression in the hippocampus of male (but not female) MAPT P301S; cTFEB;HSACre mice (Figure 4E). We confirmed activation of neurotrophic signaling in the hippocampus of male MAPT P301S;cTFEB;HSACre mice by targeted qRT-PCR analysis, which showed corrections of declining expression levels of neurotrophic factors *Bdnf* and *Fndc5* back to control littermate levels (Figures 4F and 4G).[23,55] Importantly, there was also a significant extension (38%) in the lifespan of male MAPT P301S;cTFEB;HSACre mice (Figure 4H). While the median survival of male MAPT P301S mice was 352 days (Figure 4H, teal curve), male MAPT P301S;cTFEB;HSACre mice median survival was 489 days (Figure 4H, purple curve). Although we did not detect a similar lifespan extension in female MAPT P301S; cTFEB;HSACre mice (Figure 4I), female MAPT P301S transgenic mice already live significantly longer than their male counterparts (median survival of 468.5 days), suggesting they have reached maximal lifespan in this model. Finally, we did not detect any differences in ataxia progression[56] (Figure S3D) or weight loss (Figure S3E) between our groups. These results suggest that enhanced skeletal muscle-TFEB expression modifies the accumulation of pathogenic tau isoforms, reduces neuroinflammation, and re-activates neurotrophic signaling in the hippocampus of MAPT P301S mice in a sex-dependent manner.

Skeletal muscle overexpression of TFEB decreases neuroinflammation markers and lipofuscin accumulation in the healthy aged CNS

To examine the effect of increased muscle-TFEB expression on the aging brain without neurodegenerative disease burden, we assessed the transcriptional and functional status of known inflammatory markers in the CNS of aged (20+ months old) control and cTFEB;HSACre mice, an age when global decreases in proteostasis and increases in pro-inflammatory signaling are detectable in most murine tissues,[1,57] including the CNS.[1,2] Total hippocampal mRNA levels of *Ccl2* and *Nfκb*, pro-inflammatory cytokines previously reported to mediate microglial responses to inflammation, were significantly reduced in the hippocampus of aging female (but not male) cTFEB;HSACre mice (Figures 5A and 5B). The expression of *Il6* (interleukin-6) was significantly elevated in the same group (Figure 5C). We also detected significantly higher levels of expression of *Bdnf* in hippocampal lysates from aged male (but not female) mice (Figure 5D).

Using similar morphometric analysis as before to quantify glial cell shape and morphology, we did not detect any differences in microglia (IBA1+) or astrocyte (GFAP+) number, volume, or ramification state in the dentate gyrus of aged cTFEB;HSACre bigenic mice compared with their littermate controls (Figures 5E and 5F), suggesting that the observed transcriptional expression differences may either originate in non-glial cells or not translate into detectable morphological changes at the ages examined. It is important to note that age-associated changes in neuroinflammation in an otherwise healthy brain are not as pronounced as those seen in the context of neurodegenerative disease. Overall, this suggests a shifting cytokine transcriptional landscape in the aging female cTFEB;HSACre hippocampus toward reduced pro-inflammatory signaling, consistent with what we observed in our MAPT P301S studies (Figure 4).

We examined the proteostatic clearance capabilities of the aging CNS by indirect immunofluorescence of lipofuscin (an auto-fluorescent age-associated polymer[1]) in brain sections of aged (21–24 months old) control and cTFEB;HSACre mice. While we detected striking lipofuscin granule accumulation in the aging control hippocampus (Figure 5G, top), there was a significant decrease in lipofuscin deposition in the dentate gyrus of aged cTFEB;HSACre females (Figure 5G, bottom), with a similar non-significant trend in males. We next examined the transcriptional levels of multiple autophagy and lysosomal-associated genes, and confirmed significant age-associated increases in the expression of autophagy lysosomal markers *Atg8/Lc3*, *Lamp1*, *Sqstm1*, and *Ctsd* in the male hippocampus, which has been proposed to occur as a compensation for age-associated decline in proteostasis function (Figures 5H–5K). These differences were not as prominent in the aging control female hippocampus. Some of these transcriptional increases were reduced in the hippocampus of aged male cTFEB;HSACre mice, suggesting that enhancing skeletal muscle TFEB signaling promotes maintenance of hippocampal proteostasis during aging. Our data thus indicate a potential sex bias in activation of neuroprotective signaling in the hippocampus of aging cTFEB:HSACre mice, with females showing decreased neuroinflammation (Figures 5A–5C) and males showing increased neurotrophin expression levels (Figure 5D). Our results suggest that lifelong overexpression of TFEB in skeletal muscle promotes maintenance of protein quality control in the CNS, ultimately reducing proteostatic burden and neuroinflammation in the aging hippocampus.

We next pursued neurocognitive testing in aged (16–18 months old) control and cTFEB;HSACre mice by evaluating spatial learning and memory using the Barnes maze task, a hippocampal working memory test known to be sensitive to aging in mice. We documented a significant decrease in errors per trial (Figure 5L) and significantly faster escape times (Figure 5M) in aged cTFEB;HSACre mice of both sexes compared with controls. By the last trial, cTFEB;HSACre mice escaped the maze twice as quickly as control mice. In the novel object recognition task—an independent behavioral test of hippocampal recognition memory—we also found that aged cTFEB;HSACre mice of both sexes exhibited a significantly greater number of contacts with the novel object compared with controls during the test phase (Figure 5N). Aged cTFEB;HSACre mice have around a ~15% higher preference for the novel object relative to their age-matched littermate controls (Figure 5O), without any significant differences in visual performance and motor activity between aged control and cTFEB;HSACre cohorts. These results provide exciting evidence

for a pronounced improvement in neural function in the aging brain of cTFEB;HSACre mice.

Enhancing muscle TFEB signaling transcriptionally remodels the hippocampus of cTFEB;HSACre mice in a sex-dependent manner

To determine the molecular basis of the benefits of enhancing skeletal muscle TFEB signaling on the aging CNS, we performed unbiased transcriptome analysis on hippocampal RNA lysates from young (6 months old) and aged (22–24 months old) mice (Figures 6 and 7). Bulk RNA-seq analysis revealed robust changes in gene expression in cTFEB;HSACre hippocampal RNA lysates compared with their age- and sex-matched controls (Figures 6, 7, S4, and S5). In young female cTFEB;HSACre hippocampi, we detected 618 differentially expressed genes (DEGs) (435 upregulated and 165 downregulated) (Figure 6A). Functional GO enrichment analysis showed these DEGs mapped to key categories associated with synaptic function, including ion- and voltage-gated channel activity, transporter complexes, as well as synapse and synaptic membrane categories (Figure 6C, boxes). Enrichment analysis of differential gene expression (KEGG) revealed additional critical categories associated with neural function, including oxytocin signaling, cAMP signaling, Hippo signaling, and gap junctions (Figure 6E). Furthermore, metabolic and functional pathway analysis (Reactome) also identified key categories known to regulate cognitive plasticity, including GPCR ligand binding, voltage-gated potassium channels, and transmission across chemical synapses, among others (Figure S4A).

Consistent with our biochemical and functional findings suggesting increased neuroprotective benefits in aging cTFEB;HSA-Cre mice (Figure 5), we found that these transcriptional changes modulating synaptic function pathways are still present (although not as prominent) in the aging hippocampus of aged female cTFEB;HSACre mice (Figures 6B, S4B, and S4D). Out of a total of 1,765 DEGs (541 upregulated and 1,224 downregulated), KEGG functional pathways enriched in our aged female hippocampus included categories associated with preservation of neuronal activity and cognitive function, including axon guidance, HIF-1 signaling, AMPK signaling, and PI3-Akt signaling (Figure 6F). We confirmed the age-associated differential expression of a subset of our top-hit genes in a second group of hippocampal RNA lysates using targeted qRT-PCR (Figure S4E). This suggests that overexpression of TFEB in skeletal muscle activates multiple neuroprotective gene networks associated with synaptic function and signaling in the young and aged female hippocampus.

Conversely, in the young male cTFEB;HSACre hippocampus mice we detected 471 DEGs with a 1.25-fold expression change (216 upregulated and 255 downregulated), which GO term analysis associated mostly with multiple mitochondria or ribosomal/transcription targeting pathways (Figures 7A and 7C, boxes). This included mitochondrial respiratory chain, mitochondrial protein complexes, electron transport chain, and ATP metabolic processes (Figure 7C). Additional enriched metabolic pathways in the hippocampus of young cTFEB;HSACre males included nonsense-mediated decay, metabolism of RNA, and translation (Figure S5A). Consistent with this, KEGG analysis revealed that the most enriched functional pathways were ribosomes and oxidative phosphorylation (Figure 7E).

As before, we confirmed the differential expression of a random sampling of our top-hit genes using targeted qRT-PCR (Figure S5E). When we performed similar analysis on the male aging hippocampus, we detected 539 DEGs in the hippocampus of aged male cTFEB;HSACre mice (278 upregulated, 261 downregulated) (Figure 7B), with only mild significance on functional pathways (Figures 7D, 7F, S5B, and S5D).

Further analysis also revealed that most DEGs appeared to be sex specific. Out of all DEGs in young cTFEB;HSACre hippocampi (618 in females and 471 in males), there were only 25 shared DEGs, with 16 of these changing in the same direction in both sexes (Figure S6A). A similar pattern was found in the aged cTFEB;HSACre hippocampus (1,765 total DEGs in females and 539 DEGs in males), with 39 shared DEGs and only 3 genes changing in the same direction in both sexes (Figure S6B). Our results thus strongly suggest a sex bias in the hippocampal transcriptional responses associated with muscle-TFEB overexpression, with the female hippocampi upregulating neuronal signaling and synaptic function and the male hippocampi upregulating transcriptional and mitochondrial responses. Many of these transcriptional changes are preserved until late stages in the lifespan of our model, suggesting that these changes may underlie the neurocognitive benefits observed in our aging cTFEB;HSACre cohorts.

DISCUSSION

Skeletal muscle health has recently been linked to multiple chronic age-associated conditions, including neurodegenerative diseases,[24,26] but the role of the “muscle-to-brain axis” in the these conditions remains largely unknown. Here, we provide direct evidence demonstrating the CNS benefits of enhancing muscle-TFEB expression, both during healthy aging and in the context of a neurodegenerative proteinopathy.

In addition to rescuing multiple age-associated hallmarks in skeletal muscle, we discovered that lifelong overexpression of TFEB in skeletal muscle significantly improves multiple disease-associated biochemical hallmarks in the hippocampus of cTFEB;HSACre transgenic mice. We observed robust benefits on neuroinflammation markers in the MAPT P301S model of tau toxicity, as well as a significant extension on the lifespan of male MAPT P301S;cTFEB;HSACre transgenic mice. We also report important reductions in proteotoxicity/neuroinflammation and improved neurocognitive performance in healthy aging (22–24 month old) cTFEB;HSACre mice. Importantly, these benefits arise without any detectable expression of our transgene in the CNS. Although previous work examining the muscle-to-brain axis has demonstrated important benefits on the accumulation of misfolded protein inclusions in the CNS,[5,8,19,28] similar to what we observed in the MAPT P301S;cTFEB;HSACre hippocampus, the profound reductions in neuroinflammation observed in our model suggest that modulation of skeletal muscle TFEB signaling may be a novel target to modulate neuroinflammatory signaling *in vivo* in the context of aging and/or neurodegenerative diseases.

Previous transcriptional studies of the healthy aging hippocampus have identified dysregulation of ion homeostasis, neurotransmission, and ribosome biogenesis as key biological processes associated with aging.[2,58] Genes related to synaptic transmission and

plasticity appear to be particularly sensitive to age-associated transcriptional dysregulation.[3] Many of these gene networks are also significantly altered in AD and other associated tauopathies.[55] Similar networks were transcriptionally remodeled in the healthy aging cTFEB;HSACre hippocampus, suggesting that these gene networks may be uniquely sensitive to both neurotoxic and neurotrophic signaling. Manipulation of skeletal muscle TFEB modulated expression of similar functional enrichment categories (i.e., trophic factor signaling, neuroinflammation) in the aging and tau-afflicted hippocampus of our cTFEB;HSACre mice in a sex-dependent manner. Indeed, when we compared KEGG pathways of the differentially expressed genes from the nCounter AD panel in MAPT P301S; cTFEB;HSACre hippocampus with those enriched in the hippocampus of our 24-month-old cTFEB;HSACre mice, we see shared regulation of pathways involved in axon guidance, MAPK signaling, cAMP signaling, and neuroactive ligand-receptor interactions, suggesting potential converging neurotrophic benefits associated with muscle-TFEB expression.

One of our most exciting (and unexpected) findings is the sex bias in our CNS and skeletal muscle responses to muscle-TFEB overexpression. In general, we struggled to identify previous literature thoroughly describing female-specific changes to many of the hallmarks of aging on either tissue.[1] To our surprise, while we were able to validate “classical” age-associated findings such as fiber-type switching in aging control males, these phenotypes were less robust or not present in age-matched control females, rendering interpretation of the sex bias of our CNS-targeting benefits difficult. While we observed neuroprotective effects on both male and female cTFEB;HSACre hippocampi, it appears that the mechanisms underlying these benefits are not the same. Whereas muscle-TFEB overexpression in the MAPT P301S model reduces the accumulation of hyperphosphorylated tau in both sexes, it appears to drive the transcriptional silencing of pro-inflammatory microglial signaling in females, and activates trophic factor signaling in males instead. We detected similar sex differences in our healthy aging transcriptional studies, with the female cTFEB;HSACre hippocampus activating pathways associated with synaptic function, while the male cTFEB;HSACre hippocampus activated ribosomal and mitochondrial signaling. One potential explanation could be the sex bias in TFEB expression in skeletal muscle, which is ~50% higher in male mice, suggesting a threshold effect for local remodeling of skeletal muscle. However, both sexes do display similar exercise endurance at young ages and comparable protection of mitochondrial respiration rates at old ages, suggesting converging outcomes of TFEB-mediated geroprotection of aging skeletal muscle. In our healthy aging studies, both sexes are well into the stage of reproductive senescence, which has been reported to have significant negative impacts on neural function.[59] While we did not measure circulating levels of sex hormones in our models, estrogen appears to control similar CNS signaling pathways as those differentially expressed in the hippocampus of muscle-TFEB-overexpressing female (i.e., synapse function, neurotransmitter signaling) and male (i.e., mitochondrial function) mice.[59] While it is unclear whether these differential responses between male and female hippocampi reflect local differences in the CNS itself[60] or peripheral differences in the expression, secretion, or trafficking of circulating signals, they underscore the fundamental need to examine sex differences contributing to the biology of aging and neurodegenerative diseases.[61]

Recent evidence has shown that muscle-originating circulating factors (myokines) appear to play central roles in regulating CNS function. Ctsb is secreted from skeletal muscle into circulation in response to exercise, and is required for the full manifestation of exercise-associated benefits on the CNS, including increases in hippocampal Bdnf and the activation of neurogenesis.[20] Circulating Ctsb has also been proposed to cross the blood-brain barrier,[20] and appears to remodel the extracellular matrix,[62] enhancing axonal outgrowth through degradation of chondroitin sulfate.[63,64] High Ctsb expression levels in the hippocampus have been reported in low-anxiety mouse lines,[65,66] suggesting that Ctsb may play important roles in maintaining neuronal homeostasis in brain regions with high relevance for both aging and age-associated neurodegenerative disease. Recent evidence demonstrates pronounced involvement of the macroautophagy molecular machinery in cellular secretion.[67] Cytokines associated with inflammation, such as IL-1B and IL-6, are released into the extracellular space via autophagy-dependent secretion. There is also a growing body of evidence that age[45] and exercise,[68] known modifiers of skeletal muscle metabolism, alter the composition of the skeletal muscle secretome. This suggests that activation of TFEB overexpression may be modifying the skeletal muscle secretome, potentially enriching it with neurotrophic factors or depleting it from neurotoxic factors, although this hypothesis remains to be tested.

Over the last 10 years, there has been growing evidence that suggests prominent contributions of the periphery to the etiology of neurodegenerative diseases. Our discovery that skeletal muscle TFEB signaling can be a crucial site for regulation of CNS health and function provides compelling evidence for a therapeutic delivery avenue into the brain, providing a currently unexplored diagnostic and therapeutic intervention site for preserving brain health.

Limitations of the study

Although we present evidence that enhanced skeletal muscle TFEB signaling results in the secretion of a CNS-targeting myokine that confers neuroprotection during aging and neurodegenerative disease, the precise role of Ctsb (or other secreted myokines) on the observed neuroprotective effects remains unknown. Future studies exploring the role of our differentially expressed myokines may yield interesting peripheral networks associated with brain function and health.

STAR★METHODS

Detailed methods are provided in the online version of this paper and include the following:

RESOURCE AVAILABILITY

Lead contact—Further information and requests for resources and reagents should be directed to and will be fulfilled by the lead contact, Constanza J. Cortes (cjc_149@usc.edu).

Materials availability—The fxSTOp-TFEB line of transgenic mice is available for sharing with academic institutions free-of-charge. For-profit institutions will adhere to UCSD’s policy regarding copyrighted material.

Data and code availability—Bulk RNA-seq data have been deposited at GEO (GEO: GSE242363) and are publicly available as of the date of publication. Accession numbers are listed in the key resources table. Muscle proteomics data have been deposited at Panorama Public (ID: PXD045241) and are publicly available as of the date of publication. ID numbers are listed in the key resources table. Microscopy data reported in this paper will be shared by the lead contact upon request. This paper does not report original code. Any additional information required to reanalyze the data reported in this work paper is available from the lead contact upon request.

EXPERIMENTAL MODEL AND SUBJECT PARTICIPANT DETAILS

Mouse models used were the fxSTOP-TFEB transgenic line generated for this publication, the HSA-Cre transgenic mice (JAX Strain No: 006139 | HSA-Cre79) obtained from JAX, TdTomato mice (B6.Cg-Gt(ROSA)26Sor$^{tm9(CAG\text{-}tdTomato)Hze/J}$, JAX Strain #:007909) also from JAX, and the MAPT P301S line (Stock No: 008169) which originated in the laboratory of Dr. Virginia Lee. All animals have the C57BL/6J genetic background, both males and females were used wherever possible. All animal experimentation adhered to NIH guidelines and was approved by and performed in accordance with the University of California, San Diego, Duke University, University of Alabama at Birmingham, and the University of Southern California Institutional Animal Care and Use.

METHOD DETAILS

Generation of fxSTOP-TFEB transgenic mice—We used a pCMV-human TFEB expressing vector from Origene (clone # sc122773), used previously.[27] We cloned a 3x-FLAG fragment via insertion into the Acc65I and Pac1 restriction sites of the targeting vector. The fxSTOP-TFEB vector was generated in multiple steps, as follows: (1) 5′ and 3′ targeting arms were inserted by PCR onto the ends of a minimal 1.8 kb, chloramphenicol-resistant vector; (2) an ampicillin resistance cassette was cloned into the MluI, XmaI sites of the targeting vector; (3) an 1.1 kb fragment encoding the actin promoter, a *loxP* site, a 3x-FLAG tag fused to EGFP was cloned into the NheI, PacI restriction sites of the targeting vector; (4) a 2.8 kb fragment containing the second *loxP* site, followed by 3x-FLAG-human TFEB sequence. The final fxSTOP-FLAG-human TFEB vector was microinjected into C57BL/6J:C3H/HeJ F1 hybrid oocytes. Of six founders identified, two gave rise to fxSTOP-FLAG-human TFEB lines with comparable phenotypes. Of these lines, we chose to focus our studies principally on line 419. The presence of the floxed 3x-FLAG-eGFP STOP-3x-FLAG-human TFEB cassette is verified by allele dependent qPCR genotyping analysis with each generation (Transnetyx), and expression of the 3x-FLAG-eGFP sequence (upstream of the STOP codon) in single transgenic fxSTOP-TFEB mice is assessed every other generation. We confirmed excision of 3x-FLAG-EGFP-STOP cassette in the presence of Cre-recombinase by crossing fxSTOP-TFEB transgenic female mice with HSA-Cre transgenic mice (JAX Strain No: 006139 | HSA-Cre79), and corresponds to the HSA-Cre driver mouse line from the laboratory of Dr. Judith Melki. TdTomato mice (B6.Cg-Gt(ROSA)26Sor$^{tm9(CAG\text{-}tdTomato)Hze/J}$, JAX Strain #:007909) express robust tdTomato fluorescence following Cre-mediated recombination, is congenic on the C57BL/6J genetic background and were also obtained from JAX. The MAPT P301S line (Stock No: 008169) originated in the laboratory of Dr. Virginia Lee. cTFEB; HSACre; MAPT

P301S transgenic mice were generated by crossing fxSTOP-TFEB females to MAPT P301S males. Double transgenic offspring was then crossed with heterozygote HSA-Cre transgenic individuals. All commercially available lines were obtained directly from JAX. All lines have been maintained in a C57/B6 background for over ten generations in our lab. Mice were housed in a temperature- and humidity-controlled environment on a 12-h light/dark cycle with food and water *ad libitum*. Mice of both sexes were used for all experiments in equal numbers, or as close to equal numbers as possible. For all MAPT P301 experiments, control animals are MAPT P301S; fxSTOP-TFEB−;HSACre- and/or MAPT P301S; fxSTOP-TFEB+; HSACre-littermates. For all aging experiments, control animals are fxSTOP-TFEB−;HSACre- and/or fxSTOP-TFEB+; HSACre-littermates. In our hands, we did not detect any differences on tau or aging-associated CNS phenotypes on fxSTOP-TFEB+ animals compared to the wild-type controls.

Tissue collections—Animals were anesthetized with 3.8% Avertin Solution. All animals received a transcardial perfusion with 60 mLs of cold 1x PBS. Half of CNS tissue (right/left hemi-brain) was post-fixed in 4% PFA for less than 24 h before being transferred to 30% sucrose for another 24 h before cryo-sectioning and staining the other half was micro-dissected into cortex and hippocampus and flash-frozen in liquid nitrogen for RNA and protein analyses. Half of skeletal muscle tissue (right/left limb muscle) was fresh frozen in OCT following dissection, while the other half was flash-frozen in liquid nitrogen for RNA and protein analyses.

RT-PCR analysis—Flash frozen perfused isolated mouse tissues (quadriceps, hippocampus) were placed in plastic tubes with silica beads (MP Biomedical, 116913100) and homogenized in the FastPrep-24 5G bead beating grinder and lysis system (MP Biomedical, 116005500) in TRI-zol (Invitrogen, 15596026). RNA was extracted via standard phenol-chloroform procedures followed by DNase digestion (ThermoFisher, AM2238). cDNA was generated using iScript (Bio-Rad Technologies, 1708891). Quantitative PCR was run using Sybrgreen (Life Technologies, 4309155) for chemical detection (Applied Biosystems; QuantStudio 3). Enrichment was determined based on double-delta CT value. Primers were ordered from IDT Predesigned qPCR Assays unless otherwise specified. Primers used are listed in the key resources table.

Protein extraction and immunoBlot analysis—Protein lysates from muscle tissue was prepared following standard protocols with minor modifications.[27,28] In short, flash frozen perfused isolated mouse tissues (quadriceps, hippocampus) were placed in plastic tubes with silica beads (MP Biomedical, 116913100) and homogenized in the FastPrep-24 5G bead grinder and lysis system (MP Biomedical, 116005500) in RIPA Lysis and Extraction Buffer (Invitrogen, 89900), 1X Halt Protease and Phosphatase Inhibitor Cocktail (Invitrogen, 78442), and 1% SDS. Protein concentration was quantified using a Pierce BCA Protein Assay (23227). For brain tissue, Fifty or 25 mg of homogenized proteins were loaded per lane, and after running Any KD, 10%, or 4–15% Mini-PROTEAN TGX Gels (BioRad, 4568124, 4561034, and 4561084), samples were transferred to 0.45 μm PVDF membranes (BioRad, 1704275), which were blocked in 5% BSA in PBS at RT for 1 h. For skeletal muscle, proteins were separated on 4–20% Stain-Free TGX gels

(Bio-Rad, 5678092), separated to PVDF, and blocked in 5% non-fat dry milk in TBST (1X TBS with 0.05% Tween 20) for 1 h at RT. Membranes were incubated with anti-FLAG antibody (Sigma, M2, F1804, 1:1000), anti-TFEB antibody (Cell Signaling, 4240,1:1000), anti-Lamp1 antibody (DSHB, 1DB4, 1:1000), anti-LC3A/B antibody (Cell Signaling, 12741, 1:1000), anti-P62 antibody (Cell signaling, 5114T, 1:1000), anti-ubiquitin antibody (Santa Cruz, sc-8017, 1:1000), anti-Cathepsin B antibody (Cell signaling, 3383S, 1:1000), anti-Cathepsin D antibody (Santa Cruz, sc-6486, 1:1000), or anti-GAPDH (Invitrogen, AM4300, 1:5000) in PBS-T with 5% BSA at 4°C overnight. The primary antibody was visualized with horseradish peroxidase conjugated anti-rabbit at (Cell Signaling, 7074P2, 1:5,000) and enhanced chemiluminescence (BioRad, 170-5060) or goat-*anti*-mouse IgG 680 (Invitrogen, A21058, 1:10,000). Densitometry analysis was performed using the BioRad Image Lab 6.1 software application.

Immunofluorescence studies—Tissue was embedded in OCT (TissueTek, 4583), frozen utilizing 2-methylbutane (VWR, 103525-278) submerged in liquid nitrogen and stored at −80 C until used. All samples were sectioned on a standing cryostat (Leica). Brain sections were 20 μm thick, while muscle sections were 15 μm thick. For immunohistochemistry, sections were permeabilized with .25% Triton for 15 min and blocked with 4% BSA for 30 minutes-1 hour. Brain sections were then incubated with anti-GFAP (ab4674, Abcam, 1:200), anti-IBA1 (Wako, 019-19741, 1:200), anti-AT180 TAU (ThermoFisher, MN1040, 1:100) and anti-AT8 TAU (ThermoFisher, MN1020, 1:100) while muscle sections were incubated with anti-laminin (Abcam, ab11575, 1:200), anti-FLAG (Sigma, F1804, 1:1000), anti-LC3B (Cell Signaling, 2775S, 1:200), anti-LAMP1 (Novus, NB100-77685, 1:200), anti-p62 (Progen, GP62-C, 1:200), anti-MHC Type 1 (DSHB, BD-D5, 1:100), anti-MHC Type 2A (DSHB, SC-71, 1:100), anti-MHC Type 2B (DSHB, BF-F3, 1:100), and anti-hTFFEB (CST, 4240, 1:200) overnight at 4°C and incubated with secondary antibodies at RT for 1 h (both diluted in 4% BSA). Next the slides were washed with Hoescht (ThermoFisher, 62249, 1:5000) and mounted with prolong glass (Invitrogen, P36984). All slides were washed with 1X PBS three times for 5 min each between steps.

Slides with brain sections stained for TAU and glia markers were imaged in the UAB HIRF HRIF Confocal/Light Microscopy Core utilizing the 10× objective on the Nikon A15R/SIM Confocal microscope. Z-stacks of the entire hippocampus area/section were collected, and max intensity projections were generated using FIJI. Lipofuscin imaging was performed using an epifluorescent Nikon light microscope with a 20× objective. For TdTomato imaging, stitched whole-section z-stacks were acquired using a Nikon A1R HD25 confocal microscope of nuclei in the blue channel and native TdTomato fluorescence in the red channel. Muscle sections were imaged with an ECHO Revolution epifluorescent microscope.

For quantification of astrocyte and/or microglia parameters, NIS elements was used to collect morphometric information and numbers. A size exclusion parameter was used for GFAP positive objects under 10 μm, IBA-1 positive objects under 15 μm, and any object larger than 5,000 μm were all excluded due to standard assessments of cell sizes. FIJI was used for quantification of lipofuscin and LAMP1 puncta. Muscle fibertype composition, number, and size were quantified using Myosoft,[70] a FIJI plugin.

Quantitative proteomics sample preparation and data-independent acquisition mass spectrometry ***Lysis/digestion*****—**We identified distinct protein species from crude total extractions of whole quadricep muscle by mass spectrometry. Quadricep muscle powder lysate in 50 mM ammonium bicarbonate with 0.1% RapiGest (Waters, Cat# 186001861) were processed and digested using Qiagen Tissue Lyser II (Qiagen) following the manufacturer's protocol. Protein concentrations were determined using Pierce BCA Protein Assay Kit (ThermoFisher, PI23227). 150 µg of lysate was reduced with DTT (Sigma, Cat #D0632), alkylated with IAA (Sigma, Cat #D0632) and digested at 1 µg trypsin (Thermo, Cat # PI-90057) to 50 µg protein ratio for 16 h at 37°C. Digests were acidified with 200 mM HCl (Fisher, Cat # A144), cleaned with MCX columns (Waters, Cat# 186000782), dried with a vacuum concentrator, and reconstituted in 0.1% formic acid (Fisher, Cat# A117) in water.

Liquid chromatography and mass spectrometry—One µg of each sample with 150 fmol of Pierce Retention Time Calibrant (PRTC, Thermo, Cat # PI-88321) was loaded onto a 30 cm fused silica picofrit 75 µm column (New Objective, Woburn, MA, Cat # PF3607510N5) and 3.5 cm 150 µm fused silica Kasil1 (PQ Corporation) frit trap loaded with 3 µm Reprosil-Pur C18 (ESI Source Solutions, Cat #r13.aq.0001) reverse-phase resin analyzed with a Thermo Easy nano-LC 1000 coupled to a Thermo Orbitrap Fusion Lumos Mass Spectrometer. Data-independent (DIA) mass spectrometry was performed with gas-phase fractionation.[71,72]

Data analysis—Thermo DIA MS/MS RAW files were converted to mzML format using Proteowizard (version 3.0.19045)[73] using vendor peak picking and demultiplexing. Chromatogram spectral libraries were created using default settings (10 ppm tolerances, trypsin digestion, HCD b- and y-ions) of Walnut in EncyclopeDIA (version 0.6.14)[74] using the Uniprot mouse canonical FASTA.[75] Quantitative spectral libraries were created by mapping spectral to the chromatogram spectral library using EncyclopeDIA requiring a minimum of 3 quantitative ions and filtering peptides at a 1% FDR using Percolator 3.01.[76] The quantitative spectral library is imported into Skyline-daily 4.2.1.19058[77] with the Uniprot mouse canonical FASTA as the background proteome to map peptides to proteins. The mzML data is imported and all data is TIC normalized.

Data and code availability—The Skyline document and raw files for the proteomics DIA MS/MS data are available at Panorama Public.[78] ProteomeXchange ID: PXD045241. Access URL: https://panoramaweb.org/mouse-muscle-TFEB-proteomics.url. All original data has been deposited at Panorama and is publicly available as of the date of publication. Any additional information required to reanalyze the data reported in this paper is available from the lead contact upon request.

High-resolution respirometry and ROS production—High-resolution respirometry (HRR) was conducted on a G-model Oxygraph-2k machine (Oroboros Instruments, Innsbruck, Austria). The Substrate Uncoupler Inhibitor Titration (SUIT) protocol used for HRR involves the addition of malate (2 mM) and octanoylcarnitine (0.2 mM) to 2–3 mgs of skeletal muscle tissue.[79] Antimycin A was sufficient to block complex 3 activity;

therefore, myxothiazol was not added in our SUIT protocol. ROS production was detected using the O2k-Fluo (Oroboros Instruments) and a modified Amplex Red assay. After daily background correction, chambers were closed and 20 μM final concentration Amplex Red ultra (Life Technologies, A36006), 1 U/mL horseradish peroxidase (Sigma-P8250), and 5 U/mL superoxide dismutase (Sigma-S8409) were added to the wells. After the amp-slope stabilized 0.1 μM H2O2 (Sigma-95321) was added for calibration. Throughout the entire assay, repeated injections of 0.1 μM H2O2 were used for calibration including one injection after the muscle tissue was added to correct for autofluorescence. All subsequent 0.1 μM H2O2 injections were used to control for changing concentrations of Amplex Red during the assay. Samples for HRR aere conducted in duplicate and means were used for the final analyses. To eliminate confounds from tissue damage or hyperpermeabilization, only samples with stable oxygen flux and Raw-amps were included in the final analysis.

Gene expression analysis

RNA sequencing and bioinformatics analysis: RNA was extracted as mentioned above from flash frozen hippocampal tissue for four biological replicates (sex/genotype) and checked for quality by bioAnalyzer by Novogene (Novogene Corporation INC, Sacramento, CA, United States). mRNA libraries were prepared by Novogene using poly-T oligo-attached magnetic beads. cDNA was synthesized with random hexamer primers and dUTP or dTTP depending on library directionality. For the both non-directional and directional library prep; end repair, A-tailing, adapter ligation, size selection, amplification, and purification were performed. For the directional library, end repair, USER enzyme digestion was also performed. Libraries were checked via Qubit and qPCR for quantity and by bioanalyzer for size. Quantified libraries were pooled and bulk RNA-seq analysis was performed via NovaSeq PE150 (Illumina, San Diego, CA, United States) high throughput sequencing. Bioinformatics analysis for differentially expressed genes was performed by Novogene. Raw reads were cleaned to remove adapters, poly-N and low qualities reads from the data. The reference index was built using Hisat2 v2.05 and pair-end cleaned reads were aligned to the reference genome GRCm39 through Hisat2 v2.05. reads were counted using featureCounts v1.5.0-p3. FPKM of each gene was calculated based on the length of the gene and read counts mapped. Differential expression analysis was performed using the DEseq2 R package (1.20.0). Gene Ontology (GO) and KEGG enrichment analysis of differentially expressed genes was implemented by the clusterProfiler R package. For all analysis methods and graphic representations, a p value less than 0.05 was considered significantly enriched by differentially expressed genes. For young (6-month) animals, a 2-fold change was used to determine differentially expressed genes. A 1.2-fold change was used for aged (24-month) animals. Volcano plots were generated in RStudio using ggplot2 using these criteria.

Nanostring nCounter AD panel: Assays were performed with 100 ng aliquots of RNA, extracted using the PureLink RNA extraction kit (Invitrogen) and run via the NanoString nCounter Analysis system (NanoString Technologies, Seattle, WA, USA) at the UAB Nanostring Core.[52] After codeset hybridization overnight, the samples were washed and immobilized to a cartridge using the NanoString nCounter Prep Station. Cartridges were scanned in the nCounter Digital Analyzer at 555 fields of view for the maximum level of sensitivity. Raw reads and the Nanostring Mm_AD30_v1.1 probe annotation codeset were

imported into the Nanostring proprietary software, nSolver 4.0, and QC was performed following company protocol guidelines. Counts for target genes were normalized to house-keeping genes included in the panel (Cltc, Gapdh, Gusb, Hprt, Pgk1, and Tubb5). Specifically, background correction was performed using the negative control at the cutoff of mean + 2 standard deviation. Housekeeping genes were used for normalization based on geometric mean, Gene expression was normalized using NanoStringNorm R package. All p values were adjusted using a false discovery rate (FDR) correction of 1% for multiple comparisons. Differential expression and pathway scoring analysis, as well as graphical QC representation were performed in the nSolver Advanced Analysis Software 2.0 using a custom analysis to utilize generated normalized counts. Differential gene expression values were presented asMAPT P301S baseline compared to the MAPT P301S; cTFEB; HSACre cohort for each sex, and a p value of 0.05 or less was described as significant. Volcano plots were generated with ggplot2 in Rstudio using significant genes and a cutoff of 1.2 or greater fold change. The pathway scoring module summarizes a single score from the data from a pathway's genes.[80]

Data and code availability: Bulk RNA-seq data have been deposited at GEO and are publicly available as of the date of publication. Accession numbers (GSE242363) are listed in the key resources table. No new code was generated or used in the analysis of this dataset. Any additional information required to reanalyze the data reported in this paper is available from the lead contact upon request.

Cathepsin B ELISA analysis—Fifty μL of serum (collected via blood cardiac puncture and isolated via standard coagulation/centrifugation protocols) was diluted 1:1 and processed with the Cathepsin B ELISA kit (Abcam, ab119585). Diluted samples were processed following kit instructions, and imaged at 450 nm (Tecan, Infinite M plex). Amount of cathepsin B was determined using a standard dilution curve of known concentration.

Mouse phenotyping and behavioral studies

Barnes maze—The Barnes maze apparatus is an opaque Plexiglas disc 75 cm in diameter elevated 58 cm above the floor by a tripod. Twenty holes, 5 cm in diameter, are located 5 cm from the perimeter, and a black Plexiglas escape box (19 × 8 × 7 cm) is placed under one of the holes. Distinct spatial cues are located all around the maze and are kept constant throughout the study. On the first day of testing, a training session was performed, which consists of placing the mouse in the escape box for 1 min. After the 1-min habituation period, the first session was started. At the beginning of each session, the mouse was placed in the middle of the maze in a 10 cm high cylindrical black start chamber. After 10 s the start chamber was removed, a buzzer (80 dB) and a light (400 lux) were turned on, and the mouse was set free to explore the maze. The session ended when the mouse entered the escape tunnel or after 3 min elapsed. When the mouse entered the escape tunnel, the buzzer was turned off and the mouse was allowed to remain in the dark for 1 min. When the mouse did not enter the tunnel by itself it was gently put in the escape box for 1 min. The tunnel was always located underneath the same hole (stable within the spatial environment), which was randomly determined for each mouse. Mice were tested once a day for 4 days for the

acquisition portion of the study. For the 5th test (probe test), the escape tunnel was removed and the mouse was allowed to freely explore the maze for 3 min. The time spent in each quadrant was determined and the percent time spent in the target quadrant (the one originally containing the escape box) was compared with the average percent time in the other three quadrants. This was a direct test of spatial memory as there was no potential for local cues to be used in the mouse's behavioral decision. Two weeks later the mice were tested again with the escape box in the original position (retention test). This allows for the examination of long-term memory. Finally, on the day after this test, the escape tunnel was moved to a new location (90° from the original position) and the behavior of the mouse was recorded. This is called the reversal test and it allows for the examination of perseveration at the old hole as well as the working memory strategies the mice adopted to locate the new tunnel location. Each session was videotaped and scored by an experimenter blind to the genotype of the mouse. Measures recorded include the latency to enter the escape box and the number of errors made per session. Errors are defined as nose pokes and head deflections over any hole that did not have the tunnel beneath it. The probe data were analyzed using Noldus Ethovision software to determine time spent in each quadrant of the maze as well as to assess activity measures.

Novel object recognition—Mice were individually habituated to a 51 cm × 51 cm × 39cm open field for 5 min. Mice were then tested with two identical objects placed in the field (either two 250 mL amber bottles or two clear plastic cylinders 6 × 6 × 16cm half filled with glass marbles). An individual animal was allowed to explore for 5 min, now with the objects present. After two such trials (each separated by 1 min in a holding cage), the mouse was tested in the object novelty recognition test in which a novel object replaced one of the familiar objects (for example, an amber bottle if the cylinders were initially used). All objects and the arena were thoroughly cleaned with 70% ethanol between trials to remove odors. Behavior was video recorded and then scored for number contacts (touching with nose or nose pointing at object and within 0.5 cm of object) and/or for time contacting the objects. Habituation to the objects across the familiarization trials (decreased contacts) was an initial measure of learning and then renewed interest (increased contacts) in the new object indicated successful object memory. Recognition indexes were calculated using the following formula: (# contacts during test)/(# contacts in last familiarization trial + # contacts during test). Values greater than 0.5 indicate increased interest, whereas values less than 0.5 indicate decreased interest in the object during the test relative to the final familiarization trial. quadrant of the maze as well as to assess activity measures.

QUANTIFICATION AND STATISTICAL ANALYSIS

All data were analyzed by t test, 1-way, 2-way or 3-way between-subject ANOVA with post hoc comparisons depending on the number of variables and groups in each analysis. For ANOVA, if statistical significance ($p < 0.05$) was achieved, we performed post hoc analysis to account for multiple comparisons. The level of significance (α) was always set at 0.05. Survival curves were analyzed using Log rank (Mantel-Cox) Test. Data were analyzed using Prism 7 (GraphPad Software, La Jolla, CA) and are represented as means and standard error of the means. All experiments and data analyses were conducted in a blinded fashion. All data were prepared for analysis with standard spread sheet software (Microsoft Excel).

Supplementary Material

Refer to Web version on PubMed Central for supplementary material.

ACKNOWLEDGMENTS

We thank members of the lab past and present, as well as former and current colleagues and collaborators for their helpful contributions. Funding: NIH R01 AG077536 (to C.J.C.), University of Washington Nathan Shock Center P30 AG013280 (pilot grant to C.J.C.), San Antonio Nathan Shock Center of Excellence in the Basic Biology of Aging P30 AG013319 (pilot grant to C.J.C.), NIA T32 AG052374 (training grant to I.M. and A.B.), and NIH R35 122140 (to A.R.L.S.).

INCLUSION AND DIVERSITY

One or more of the authors of this paper self-identifies as an underrepresented ethnic minority in their field of research or within their geographical location. One or more of the authors of this paper received support from a program designed to increase minority representation in their field of research. While citing references scientifically relevant for this work, we also actively worked to promote gender balance in our reference list. We worked to ensure sex balance in the selection of non-human subjects.

REFERENCES

1. López-Otín C, Blasco MA, Partridge L, Serrano M, and Kroemer G (2023). Hallmarks of aging: An expanding universe. Cell 186, 243–278. 10.1016/j.cell.2022.11.001. [PubMed: 36599349]
2. Mattson MP, and Arumugam TV (2018). Hallmarks of Brain Aging: Adaptive and Pathological Modification by Metabolic States. Cell Metab. 27, 1176–1199. 10.1016/j.cmet.2018.05.011. [PubMed: 29874566]
3. Ham S, and Lee SJV (2020). Advances in transcriptome analysis of human brain aging. Exp. Mol. Med. 52, 1787–1797. 10.1038/s12276-020-00522-6. [PubMed: 33244150]
4. Demontis F, Patel VK, Swindell WR, and Perrimon N (2014). Intertissue control of the nucleolus via a myokine-dependent longevity pathway. Cell Rep. 7, 1481–1494. 10.1016/j.celrep.2014.05.001. [PubMed: 24882005]
5. Rai M, Coleman Z, Curley M, Nityanandam A, Platt A, Robles-Murguia M, Jiao J, Finkelstein D, Wang YD, Xu B, et al. (2021). Proteasome stress in skeletal muscle mounts a long-range protective response that delays retinal and brain aging. Cell Metab. 33, 1137–1154.e9. 10.1016/j.cmet.2021.03.005. [PubMed: 33773104]
6. Durieux J, Wolff S, and Dillin A (2011). The cell-non-autonomous nature of electron transport chain-mediated longevity. Cell 144, 79–91. 10.1016/j.cell.2010.12.016. [PubMed: 21215371]
7. Taylor RC, and Dillin A (2013). XBP-1 is a cell-nonautonomous regulator of stress resistance and longevity. Cell 153, 1435–1447. 10.1016/j.cell.2013.05.042. [PubMed: 23791175]
8. Demontis F, and Perrimon N (2010). FOXO/4E-BP signaling in Drosophila muscles regulates organism-wide proteostasis during aging. Cell 143, 813–825. 10.1016/j.cell.2010.10.007. [PubMed: 21111239]
9. van Oosten-Hawle P, Porter RS, and Morimoto RI (2013). Regulation of organismal proteostasis by transcellular chaperone signaling. Cell 153, 1366–1378. 10.1016/j.cell.2013.05.015. [PubMed: 23746847]
10. Villeda SA, Luo J, Mosher KI, Zou B, Britschgi M, Bieri G, Stan TM, Fainberg N, Ding Z, Eggel A, et al. (2011). The ageing systemic milieu negatively regulates neurogenesis and cognitive function. Nature 477, 90–94. 10.1038/nature10357. [PubMed: 21886162]
11. Conboy IM, Conboy MJ, Wagers AJ, Girma ER, Weissman IL, and Rando TA (2005). Rejuvenation of aged progenitor cells by exposure to a young systemic environment. Nature 433, 760–764. 10.1038/nature03260. [PubMed: 15716955]

12. Castellano JM, Mosher KI, Abbey RJ, McBride AA, James ML, Berdnik D, Shen JC, Zou B, Xie XS, Tingle M, et al. (2017). Human umbilical cord plasma proteins revitalize hippocampal function in aged mice. Nature 544, 488–492. 10.1038/nature22067. [PubMed: 28424512]
13. Schaum N, Lehallier B, Hahn O, Pálovics R, Hosseinzadeh S, Lee SE, Sit R, Lee DP, Losada PM, Zardeneta ME, et al. (2020). Ageing hallmarks exhibit organ-specific temporal signatures. Nature 583, 596–602. 10.1038/s41586-020-2499-y. [PubMed: 32669715]
14. Villeda SA, Plambeck KE, Middeldorp J, Castellano JM, Mosher KI, Luo J, Smith LK, Bieri G, Lin K, Berdnik D, et al. (2014). Young blood reverses age-related impairments in cognitive function and synaptic plasticity in mice. Nat. Med. 20, 659–663. 10.1038/nm.3569. [PubMed: 24793238]
15. De Miguel Z, Khoury N, Betley MJ, Lehallier B, Willoughby D, Olsson N, Yang AC, Hahn O, Lu N, Vest RT, et al. (2021). Exercise plasma boosts memory and dampens brain inflammation via clusterin. Nature 600, 494–499. 10.1038/s41586-021-04183-x. [PubMed: 34880498]
16. Horowitz AM, Fan X, Bieri G, Smith LK, Sanchez-Diaz CI, Schroer AB, Gontier G, Casaletto KB, Kramer JH, Williams KE, and Villeda SA (2020). Blood factors transfer beneficial effects of exercise on neurogenesis and cognition to the aged brain. Science 369, 167–173. 10.1126/science.aaw2622. [PubMed: 32646997]
17. Ozek C, Krolewski RC, Buchanan SM, and Rubin LL (2018). Growth Differentiation Factor 11 treatment leads to neuronal and vascular improvements in the hippocampus of aged mice. Sci. Rep. 8, 17293. 10.1038/s41598-018-35716-6. [PubMed: 30470794]
18. Wrann CD, White JP, Salogiannnis J, Laznik-Bogoslavski D, Wu J, Ma D, Lin JD, Greenberg ME, and Spiegelman BM (2013). Exercise induces hippocampal BDNF through a PGC-1α/FNDC5 pathway. Cell Metab. 18, 649–659. 10.1016/j.cmet.2013.09.008. [PubMed: 24120943]
19. Islam MR, Valaris S, Young MF, Haley EB, Luo R, Bond SF, Mazuera S, Kitchen RR, Caldarone BJ, Bettio LEB, et al. (2021). Exercise hormone irisin is a critical regulator of cognitive function. Nat. Metab. 3, 1058–1070. 10.1038/s42255-021-00438-z (2021. [PubMed: 34417591]
20. Moon HY, Becke A, Berron D, Becker B, Sah N, Benoni G, Janke E, Lubejko ST, Greig NH, Mattison JA, et al. (2016). Running-Induced Systemic Cathepsin B Secretion Is Associated with Memory Function. Cell Metab. 24, 332–340. 10.1016/j.cmet.2016.05.025. [PubMed: 27345423]
21. White PJ, St-Pierre P, Charbonneau A, Mitchell PL, St-Amand E, Marcotte B, and Marette A (2014). Protectin DX alleviates insulin resistance by activating a myokine-liver glucoregulatory axis. Nat. Med. 20, 664–669. 10.1038/nm.3549. [PubMed: 24813250]
22. Quinn LS, Anderson BG, Strait-Bodey L, Stroud AM, and Argilés JM (2009). Oversecretion of interleukin-15 from skeletal muscle reduces adiposity. Am. J. Physiol. Endocrinol. Metab. 296, E191–E202. [PubMed: 19001550]
23. Lourenco MV, Frozza RL, de Freitas GB, Zhang H, Kincheski GC, Ribeiro FC, Gonçalves RA, Clarke JR, Beckman D, Staniszewski A, et al. (2019). Exercise-linked FNDC5/irisin rescues synaptic plasticity and memory defects in Alzheimer's models. Nat. Med. 25, 165–175. 10.1038/s41591-018-0275-4. [PubMed: 30617325]
24. Gupta R, Khan R, and Cortes CJ (2021). Forgot to Exercise? Exercise Derived Circulating Myokines in Alzheimer's Disease: A Perspective. Front. Neurol. 12, 649452. 10.3389/fneur.2021.649452. [PubMed: 34276532]
25. Boyle PA, Buchman AS, Wilson RS, Leurgans SE, and Bennett DA (2009). Association of muscle strength with the risk of Alzheimer disease and the rate of cognitive decline in community-dwelling older persons. Arch. Neurol. 66, 1339–1344. 10.1001/archneurol.2009.240. [PubMed: 19901164]
26. Kim J, Choi KH, Cho SG, Kang SR, Yoo SW, Kwon SY, Min JJ, Bom HS, and Song HC (2019). Association of muscle and visceral adipose tissues with the probability of Alzheimer's disease in healthy subjects. Sci. Rep. 9, 949. 10.1038/s41598-018-37244-9. [PubMed: 30700801]
27. Cortes CJ, Miranda HC, Frankowski H, Batlevi Y, Young JE, Le A, Ivanov N, Sopher BL, Carromeu C, Muotri AR, et al. (2014). Polyglutamine-expanded androgen receptor interferes with TFEB to elicit autophagy defects in SBMA. Nat. Neurosci. 17, 1180–1189. 10.1038/nn.3787. [PubMed: 25108912]

28. Cortes CJ, Ling SC, Guo LT, Hung G, Tsunemi T, Ly L, Tokunaga S, Lopez E, Sopher BL, Bennett CF, et al. (2014). Muscle expression of mutant androgen receptor accounts for systemic and motor neuron disease phenotypes in spinal and bulbar muscular atrophy. Neuron 82, 295–307. 10.1016/j.neuron.2014.03.001. [PubMed: 24742458]
29. Lieberman AP, Yu Z, Murray S, Peralta R, Low A, Guo S, Yu XX, Cortes CJ, Bennett CF, Monia BP, et al. (2014). Peripheral androgen receptor gene suppression rescues disease in mouse models of spinal and bulbar muscular atrophy. Cell Rep. 7, 774–784. 10.1016/j.celrep.2014.02.008. [PubMed: 24746732]
30. Settembre C, Di Malta C, Polito VA, Garcia Arencibia M, Vetrini F, Erdin S, Erdin SU, Huynh T, Medina D, Colella P, et al. (2011). TFEB links autophagy to lysosomal biogenesis. Science 332, 1429–1433. 10.1126/science.1204592. [PubMed: 21617040]
31. Palmieri M, Impey S, Kang H, di Ronza A, Pelz C, Sardiello M, and Ballabio A (2011). Characterization of the CLEAR network reveals an integrated control of cellular clearance pathways. Hum. Mol. Genet. 20, 3852–3866. 10.1093/hmg/ddr306. [PubMed: 21752829]
32. Sardiello M, Palmieri M, di Ronza A, Medina DL, Valenza M, Gennarino VA, Di Malta C, Donaudy F, Embrione V, Polishchuk RS, et al. (2009). A gene network regulating lysosomal biogenesis and function. Science 325, 473–477. 10.1126/science.1174447. [PubMed: 19556463]
33. Morgan TE, Xie Z, Goldsmith S, Yoshida T, Lanzrein AS, Stone D, Rozovsky I, Perry G, Smith MA, and Finch CE (1999). The mosaic of brain glial hyperactivity during normal ageing and its attenuation by food restriction. Neuroscience 89, 687–699. 10.1016/s0306-4522(98)00334-0. [PubMed: 10199605]
34. Settembre C, De Cegli R, Mansueto G, Saha PK, Vetrini F, Visvikis O, Huynh T, Carissimo A, Palmer D, Klisch TJ, et al. (2013). TFEB controls cellular lipid metabolism through a starvation-induced autoregulatory loop. Nat. Cell Biol. 15, 647–658. 10.1038/ncb2718. [PubMed: 23604321]
35. van Praag H, Shubert T, Zhao C, and Gage FH (2005). Exercise enhances learning and hippocampal neurogenesis in aged mice. J. Neurosci. 25, 8680–8685. 10.1523/jneurosci.1731-05.2005. [PubMed: 16177036]
36. Mansueto G, Armani A, Viscomi C, D'Orsi L, De Cegli R, Polishchuk EV, Lamperti C, Di Meo I, Romanello V, Marchet S, et al. (2017). Transcription Factor EB Controls Metabolic Flexibility during Exercise. Cell Metab. 25, 182–196. 10.1016/j.cmet.2016.11.003. [PubMed: 28011087]
37. Leu M, Bellmunt E, Schwander M, Fariñas I, Brenner HR, and Müller U (2003). Erbb2 regulates neuromuscular synapse formation and is essential for muscle spindle development. Development 130, 2291–2301. [PubMed: 12702645]
38. Masiero E, Agatea L, Mammucari C, Blaauw B, Loro E, Komatsu M, Metzger D, Reggiani C, Schiaffino S, and Sandri M (2009). Autophagy is required to maintain muscle mass. Cell Metab. 10, 507–515. 10.1016/j.cmet.2009.10.008. [PubMed: 19945408]
39. Kustermann M, Manta L, Paone C, Kustermann J, Lausser L, Wiesner C, Eichinger L, Clemen CS, Schröder R, Kestler HA, et al. (2018). Loss of the novel Vcp (valosin containing protein) interactor Washc4 interferes with autophagy-mediated proteostasis in striated muscle and leads to myopathy in vivo. Autophagy 14, 1911–1927. 10.1080/15548627.2018.1491491. [PubMed: 30010465]
40. Giacomello E, Crea E, Torelli L, Bergamo A, Reggiani C, Sava G, and Toniolo L (2020). Age Dependent Modification of the Metabolic Profile of the Tibialis Anterior Muscle Fibers in C57BL/6J Mice. Int. J. Mol. Sci. 21, 3923. 10.3390/ijms21113923. [PubMed: 32486238]
41. Szklarczyk D, Gable AL, Nastou KC, Lyon D, Kirsch R, Pyysalo S, Doncheva NT, Legeay M, Fang T, Bork P, et al. (2021). The STRING database in 2021: customizable protein-protein networks, and functional characterization of user-uploaded gene/measurement sets. Nucleic Acids Res. 49, D605–D612. 10.1093/nar/gkaa1074. [PubMed: 33237311]
42. Spampanato C, Feeney E, Li L, Cardone M, Lim JA, Annunziata F, Zare H, Polishchuk R, Puertollano R, Parenti G, et al. (2013). Transcription factor EB (TFEB) is a new therapeutic target for Pompe disease. EMBO Mol. Med. 5, 691–706. 10.1002/emmm.201202176. [PubMed: 23606558]
43. Valentine JM, Li ME, Shoelson SE, Zhang N, Reddick RL, and Musi N (2020). NFkappaB Regulates Muscle Development and Mitochondrial Function. J. Gerontol. A Biol. Sci. Med. Sci. 75, 647–653. 10.1093/gerona/gly262. [PubMed: 30423026]

44. Rai M, and Demontis F (2016). Systemic Nutrient and Stress Signaling via Myokines and Myometabolites. Annu. Rev. Physiol. 78, 85–107. 10.1146/annurev-physiol-021115-105305. [PubMed: 26527185]
45. Mancinelli R, Checcaglini F, Coscia F, Gigliotti P, Fulle S, and Fanò-Illic G (2021). Biological Aspects of Selected Myokines in Skeletal Muscle: Focus on Aging. Int. J. Mol. Sci. 22, 8520. 10.3390/ijms22168520. [PubMed: 34445222]
46. Cortazar AR, Oguiza JA, Aransay AM, and Lavin JL (2017). VerSeDa: Vertebrate Secretome Database. Database 2017, baw171. 10.1093/database/baw171. [PubMed: 28365718]
47. Yoshiyama Y, Higuchi M, Zhang B, Huang SM, Iwata N, Saido TC, Maeda J, Suhara T, Trojanowski JQ, and Lee VMY (2007). Synapse loss and microglial activation precede tangles in a P301S tauopathy mouse model. Neuron 53, 337–351. 10.1016/j.neuron.2007.01.010. [PubMed: 17270732]
48. Moloney CM, Lowe VJ, and Murray ME (2021). Visualization of neurofibrillary tangle maturity in Alzheimer's disease: A clinicopathologic perspective for biomarker research. Alzheimers Dement. 17, 1554–1574. 10.1002/alz.12321. [PubMed: 33797838]
49. Jurga AM, Paleczna M, and Kuter KZ (2020). Overview of General and Discriminating Markers of Differential Microglia Phenotypes. Front. Cell. Neurosci. 14, 198. 10.3389/fncel.2020.00198. [PubMed: 32848611]
50. Godbout JP, Chen J, Abraham J, Richwine AF, Berg BM, Kelley KW, and Johnson RW (2005). Exaggerated neuroinflammation and sickness behavior in aged mice following activation of the peripheral innate immune system. FASEB J. 19, 1329–1331. 10.1096/fj.05-3776fje. [PubMed: 15919760]
51. Sidoryk-Wegrzynowicz M, Gerber YN, Ries M, Sastre M, Tolkovsky AM, and Spillantini MG (2017). Astrocytes in mouse models of tauopathies acquire early deficits and lose neurosupportive functions. Acta Neuropathol. Commun. 5, 89. 10.1186/s40478-017-0478-9. [PubMed: 29187256]
52. Preuss C, Pandey R, Piazza E, Fine A, Uyar A, Perumal T, Garceau D, Kotredes KP, Williams H, Mangravite LM, et al. (2020). A novel systems biology approach to evaluate mouse models of late-onset Alzheimer's disease. Mol. Neurodegener. 15, 67. 10.1186/s13024-020-00412-5. [PubMed: 33172468]
53. Simon MJ, Wang MX, Murchison CF, Roese NE, Boespflug EL, Woltjer RL, and Iliff JJ (2018). Transcriptional network analysis of human astrocytic endfoot genes reveals region-specific associations with dementia status and tau pathology. Sci. Rep. 8, 12389. 10.1038/s41598-018-30779-x. [PubMed: 30120299]
54. Sherva R, Tripodis Y, Bennett DA, Chibnik LB, Crane PK, de Jager PL, Farrer LA, Saykin AJ, Shulman JM, Naj A, et al. (2014). Genome-wide association study of the rate of cognitive decline in Alzheimer's disease. Alzheimers Dement. 10, 45–52. 10.1016/j.jalz.2013.01.008. [PubMed: 23535033]
55. Knopman DS, Amieva H, Petersen RC, Chételat G, Holtzman DM, Hyman BT, Nixon RA, and Jones DT (2021). Alzheimer disease. Nat. Rev. Dis. Primers 7, 33. 10.1038/s41572-021-00269-y (2021. [PubMed: 33986301]
56. Guyenet SJ, Furrer SA, Damian VM, Baughan TD, La Spada AR, and Garden GA (2010). A simple composite phenotype scoring system for evaluating mouse models of cerebellar ataxia. J. Vis. Exp. 39, 1787. 10.3791/1787.
57. Lehallier B, Gate D, Schaum N, Nanasi T, Lee SE, Yousef H, Moran Losada P, Berdnik D, Keller A, Verghese J, et al. (2019). Undulating changes in human plasma proteome profiles across the lifespan. Nat. Med. 25, 1843–1850. 10.1038/s41591-019-0673-2. [PubMed: 31806903]
58. Ximerakis M, Lipnick SL, Innes BT, Simmons SK, Adiconis X, Dionne D, Mayweather BA, Nguyen L, Niziolek Z, Ozek C, et al. (2019). Single-cell transcriptomic profiling of the aging mouse brain. Nat. Neurosci. 22, 1696–1708. 10.1038/s41593-019-0491-3. [PubMed: 31551601]
59. Zárate S, Stevnsner T, and Gredilla R (2017). Role of Estrogen and Other Sex Hormones in Brain Aging. Neuroprotection and DNA Repair. Front. Aging Neurosci. 9, 430. 10.3389/fnagi.2017.00430. [PubMed: 29311911]

60. Hahn O, Foltz AG, Atkins M, Kedir B, Moran-Losada P, Guldner IH, Munson C, Kern F, Pálovics R, Lu N, et al. (2023). Atlas of the aging mouse brain reveals white matter as vulnerable foci. Cell 186, 4117–4133.e22. 10.1016/j.cell.2023.07.027. [PubMed: 37591239]
61. Cortes CJ, and De Miguel Z (2022). Precision Exercise Medicine: Sex Specific Differences in Immune and CNS Responses to Physical Activity. Brain Plast. 8, 1–13. 10.3233/BPL-220139. [PubMed: 36448037]
62. Vizovišek M, Fonovic M., and Turk B. (2019). Cysteine cathepsins in extracellular matrix remodeling: Extracellular matrix degradation and beyond. Matrix Biol. 75–76, 141–159. 10.1016/j.matbio.2018.01.024.
63. Tran AP, Sundar S, Yu M, Lang BT, and Silver J (2018). Modulation of Receptor Protein Tyrosine Phosphatase Sigma Increases Chondroitin Sulfate Proteoglycan Degradation through Cathepsin B Secretion to Enhance Axon Outgrowth. J. Neurosci. 38, 5399–5414. 10.1523/JNEUROSCI.3214-17.2018. [PubMed: 29760175]
64. Saini MG, and Bix GJ (2012). Oxygen-glucose deprivation (OGD) and interleukin-1 (IL-1) differentially modulate cathepsin B/L mediated generation of neuroprotective perlecan LG3 by neurons. Brain Res. 1438, 65–74. 10.1016/j.brainres.2011.12.027. [PubMed: 22244880]
65. Muigg P, Scheiber S, Salchner P, Bunck M, Landgraf R, and Singewald N (2009). Differential stress-induced neuronal activation patterns in mouse lines selectively bred for high, normal or low anxiety. PLoS One 4, e5346. 10.1371/journal.pone.0005346. [PubMed: 19399175]
66. Czibere L, Baur LA, Wittmann A, Gemmeke K, Steiner A, Weber P, Pütz B, Ahmad N, Bunck M, Graf C, et al. (2011). Profiling trait anxiety: transcriptome analysis reveals cathepsin B (Ctsb) as a novel candidate gene for emotionality in mice. PLoS One 6, e23604. 10.1371/journal.pone.0023604. [PubMed: 21897848]
67. New J, and Thomas SM (2019). Autophagy-dependent secretion: mechanism, factors secreted, and disease implications. Autophagy 15, 1682–1693. 10.1080/15548627.2019.1596479. [PubMed: 30894055]
68. Chow LS, Gerszten RE, Taylor JM, Pedersen BK, van Praag H, Trappe S, Febbraio MA, Galis ZS, Gao Y, Haus JM, et al. (2022). Exerkines in health, resilience and disease. Nat. Rev. Endocrinol. 18, 273–289. 10.1038/s41574-022-00641-2. [PubMed: 35304603]
69. Schindelin J, Arganda-Carreras I, Frise E, Kaynig V, Longair M, Pietzsch T, Preibisch S, Rueden C, Saalfeld S, Schmid B, et al. (2012). Fiji: an open-source platform for biological-image analysis. Nat. Methods 9, 676–682. 10.1038/nmeth.2019. [PubMed: 22743772]
70. Encarnacion-Rivera L, Foltz S, Hartzell HC, and Choo H (2020). An automated muscle histology analysis tool using machine learning algorithm utilizing FIJI/ImageJ software. PLoS One 15, e0229041. 10.1371/journal.pone.0229041. [PubMed: 32130242]
71. Herrera JJ, Louzon S, Pifer K, Leander D, Merrihew GE, Park JH, Szczesniak K, Whitson J, Wilkinson JE, Fiehn O, et al. (2020). Acarbose has sex-dependent and -independent effects on age-related physical function, cardiac health, and lipid biology. JCI Insight 5, e137474. 10.1172/jci.insight.137474. [PubMed: 32990683]
72. Amodei D, Egertson J, MacLean BX, Johnson R, Merrihew GE, Keller A, Marsh D, Vitek O, Mallick P, and MacCoss MJ (2019). Improving Precursor Selectivity in Data-Independent Acquisition Using Overlapping Windows. J. Am. Soc. Mass Spectrom. 30, 669–684. 10.1007/s13361-018-2122-8. [PubMed: 30671891]
73. Adusumilli R, and Mallick P (2017). Data Conversion with ProteoWizard msConvert. Methods Mol. Biol. 1550, 339–368. 10.1007/978-1-4939-6747-6_23.
74. Searle BC, Pino LK, Egertson JD, Ting YS, Lawrence RT, MacLean BX, Villén J, and MacCoss MJ (2018). Chromatogram libraries improve peptide detection and quantification by data independent acquisition mass spectrometry. Nat. Commun. 9, 5128. 10.1038/s41467-018-07454-w. [PubMed: 30510204]
75. Wu CH, Apweiler R, Bairoch A, Natale DA, Barker WC, Boeckmann B, Ferro S, Gasteiger E, Huang H, Lopez R, et al. (2006). The Universal Protein Resource (UniProt): an expanding universe of protein information. Nucleic Acids Res. 34, D187–D191. 10.1093/nar/gkj161. [PubMed: 16381842]

76. Käll L, Canterbury JD, Weston J, Noble WS, and MacCoss MJ (2007). Semi-supervised learning for peptide identification from shotgun proteomics datasets. Nat. Methods 4, 923–925. 10.1038/nmeth1113. [PubMed: 17952086]

77. MacLean B, Tomazela DM, Shulman N, Chambers M, Finney GL, Frewen B, Kern R, Tabb DL, Liebler DC, and MacCoss MJ (2010). Skyline: an open source document editor for creating and analyzing targeted proteomics experiments. Bioinformatics 26, 966–968. 10.1093/bioinformatics/btq054. [PubMed: 20147306]

78. Sharma V, Eckels J, Schilling B, Ludwig C, Jaffe JD, MacCoss MJ, and MacLean B (2018). Panorama Public: A Public Repository for Quantitative Data Sets Processed in Skyline. Mol. Cell. Proteomics 17, 1239–1244. 10.1074/mcp.RA117.000543. [PubMed: 29487113]

79. Pesta D, Hoppel F, Macek C, Messner H, Faulhaber M, Kobel C, Parson W, Burtscher M, Schocke M, and Gnaiger E (2011). Similar qualitative and quantitative changes of mitochondrial respiration following strength and endurance training in normoxia and hypoxia in sedentary humans. Am. J. Physiol. Regul. Integr. Comp. Physiol. 301, R1078–R1087. 10.1152/ajpregu.00285.2011. [PubMed: 21775647]

80. Tomfohr J, Lu J, and Kepler TB (2005). Pathway level analysis of gene expression using singular value decomposition. BMC Bioinf. 6, 225. 10.1186/1471-2105-6-225.

Highlights

- Increased TFEB expression modifies aging hallmarks in skeletal muscle
- Muscle-TFEB reduces neuroinflammation during aging and neurodegeneration
- Neuroprotective muscle-to-brain signaling is activated in a sex-biased manner

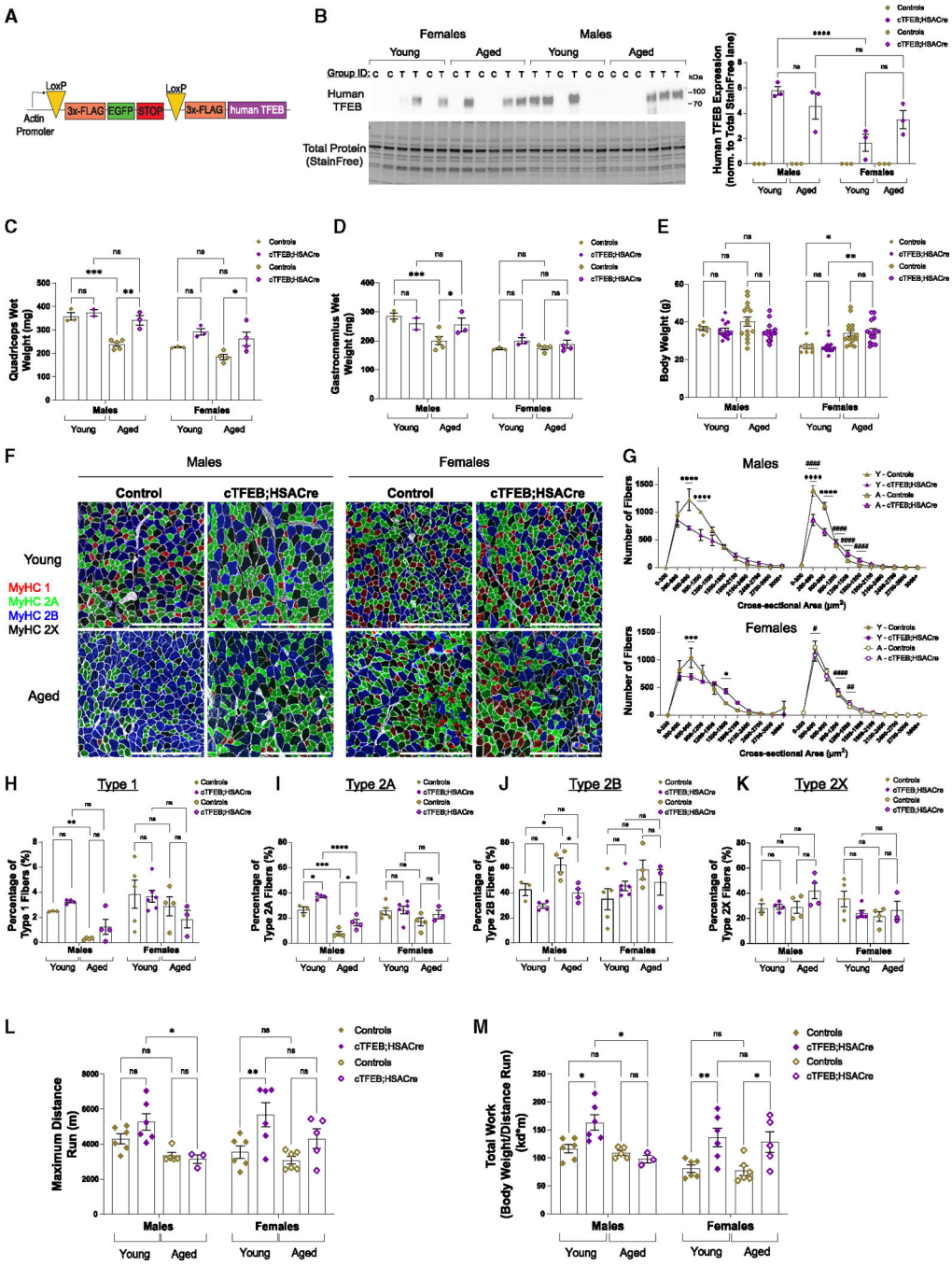

Figure 1. Skeletal muscle overexpression of TFEB preserves muscle size, fiber type composition, and increases exercise endurance during aging

(A) Schematic depicting 3x-FLAG human TFEB transgene. Cassettes are arranged from 5′ (left) to 3′ (right). The 3x-FLAG-EGFP-STOP cassette (flanked by *loxP* sites) prevents expression of the 3x-FLAG human TFEB transgene unless in the presence of Cre recombinase.

(B) Immunoblot of control and cTFEB;HSACre quadriceps confirming 3x-FLAG-TFEB protein expression in young (5–6 months) and aged (22–24 months) mice of both sexes. C, control; T, cTFEB;HSACre individuals. Transgenic 3x-FLAG-TFEB protein weighs ~75

kDa. Total protein stain-free lanes are shown below as a loading control. Densitometry quantification relative to average of young male control individuals.

(C−E) Skeletal muscle (quadriceps, C, and gastrocnemius, D) wet weight and body weight (E) in young (6 months) and aged (22–24 months) control and cTFEB;HSACre mice of both sexes.

(F) Gastrocnemius cross-sections in young (7–9 months) and aged (22–24 months) control and cTFEB;HSACre transgenic mice of both sexes. MyHC1 (fiber type 1) in red, MyHC2A (fiber type 2A) in green, MyHC2B (fiber type 2B) in blue, MyHC2X (fiber type 2x) unstained, and laminin in white. Scale bars, 500 μm.

(G−K) Fiber cross-sectional area distribution curves (G) and quantifications of each fiber type percentage (H–K) from (F). *Statistical difference between control and cTFEB;HSACre. #Statistical difference between young and aged controls. Each data point represents the average of three separate images collected from three sections/individual.

(L and M) High-intensity exhaustive treadmill exercise of young (6 months) and aged (18 months) control and cTFEB;HSACre transgenic mice of both sexes showing maximum distance run until exhaustion (L) and total work (body weight/distance run) (M). Controls are age-matched littermates. Unless otherwise stated, data are presented as mean ± SEM. $^{*/\#}p < 0.05$, $^{**/\#\#}p < 0.01$, $^{****/\#\#\#\#}p < 0.0001$ ANOVA and post-hoc multiple comparisons for each sex. Lack of annotation indicates comparisons were not significant.

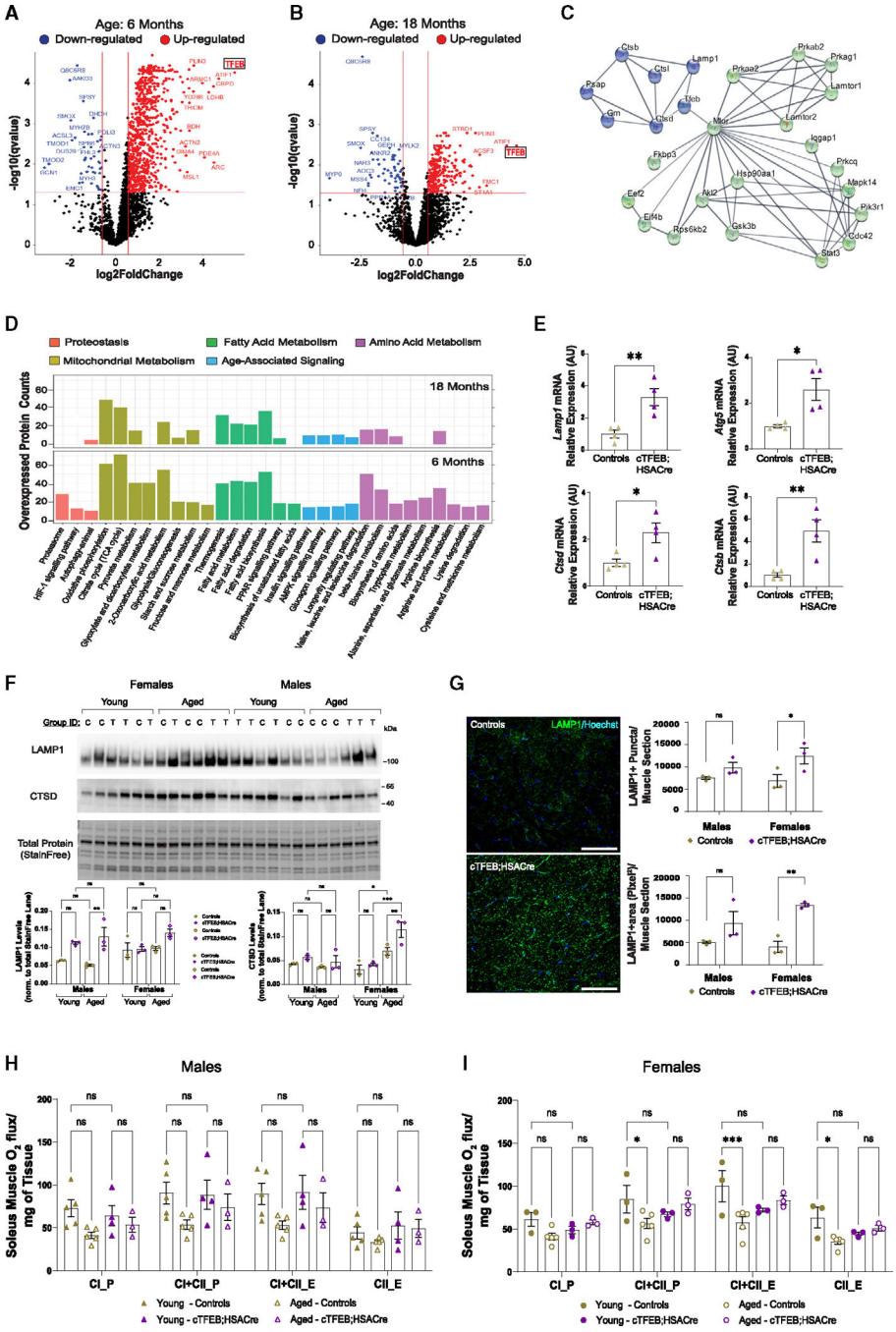

Figure 2. Muscle TFEB overexpression increases lysosomal network size and preserves mitochondrial function during aging

(A and B) Volcano plot of differentially expressed proteins in young (A) (6 months old) and aged (B) (18 months old) cTFEB;HSACre quadriceps relative to controls. Upregulated proteins in red, downregulated proteins in blue.

(C) STRING-predicted protein-protein interactions of overexpressed proteins from (A) showing interacting networks converging on TFEB (blue) and mTOR (green).

(D) KEGG enrichment analysis clusters overexpressed proteins from (A and B) into categories associated with proteostasis and autophagy (orange), mitochondrial metabolism

(gold), fatty acid metabolism (green), age-associated signaling (blue), and amino acid metabolism (purple).

(E) qRT-PCR for *Lamp1*, *Atg5*, *Ctsd*, and *CtsB* expression in quadriceps mRNA lysates from young (6 months old) male cTFEB;HSACre mice and controls.

(F) Immunoblot analysis for LAMP1 and cathepsin D from young (5–6 months) and aged (22–24 months) control and cTFEB;HSACre quadriceps lysates from mice of both sexes. Total protein stain-free lanes are shown as a loading control. Marker densitometry quantification relative to protein stain-free densitometry shown below.

(G) Gastrocnemius cross-sections from young (6–7 months old) control and cTFEB;HSACre female mice stained for LAMP1 (green), Hoechst (blue). Quantification of LAMP1+ puncta and LAMP1+ area/muscle section for both sexes (right). Scale bars, 100 μm.

(H and I) Mitochondrial function measured by oxygen flux normalized to citrate synthase activity in soleus muscle from young (6 months old) and aged (18 months old) male (H) and female (I) control and cTFEB;HSACre semi-permeabilized soleus muscle. CI_P is complex I and CI + CII_P is complex I and II linked respiration coupled to ATP production. CI + CII_E is uncoupled complex I and II respiration or maximum respiration. CII_E is complex II respiration in the uncoupled state. Each point represents the average of all data collected from an individual. Controls are age-matched littermates. All data were analyzed by two-way between-subject (age × genotype) ANOVA with post hoc multiple comparisons, or one-way ANOVA and multiple comparisons post hoc for each sex. Data are presented as mean ± SEM. *$p < 0.05$, **$p < 0.01$. Lack of annotation indicates that comparisons were not significant.

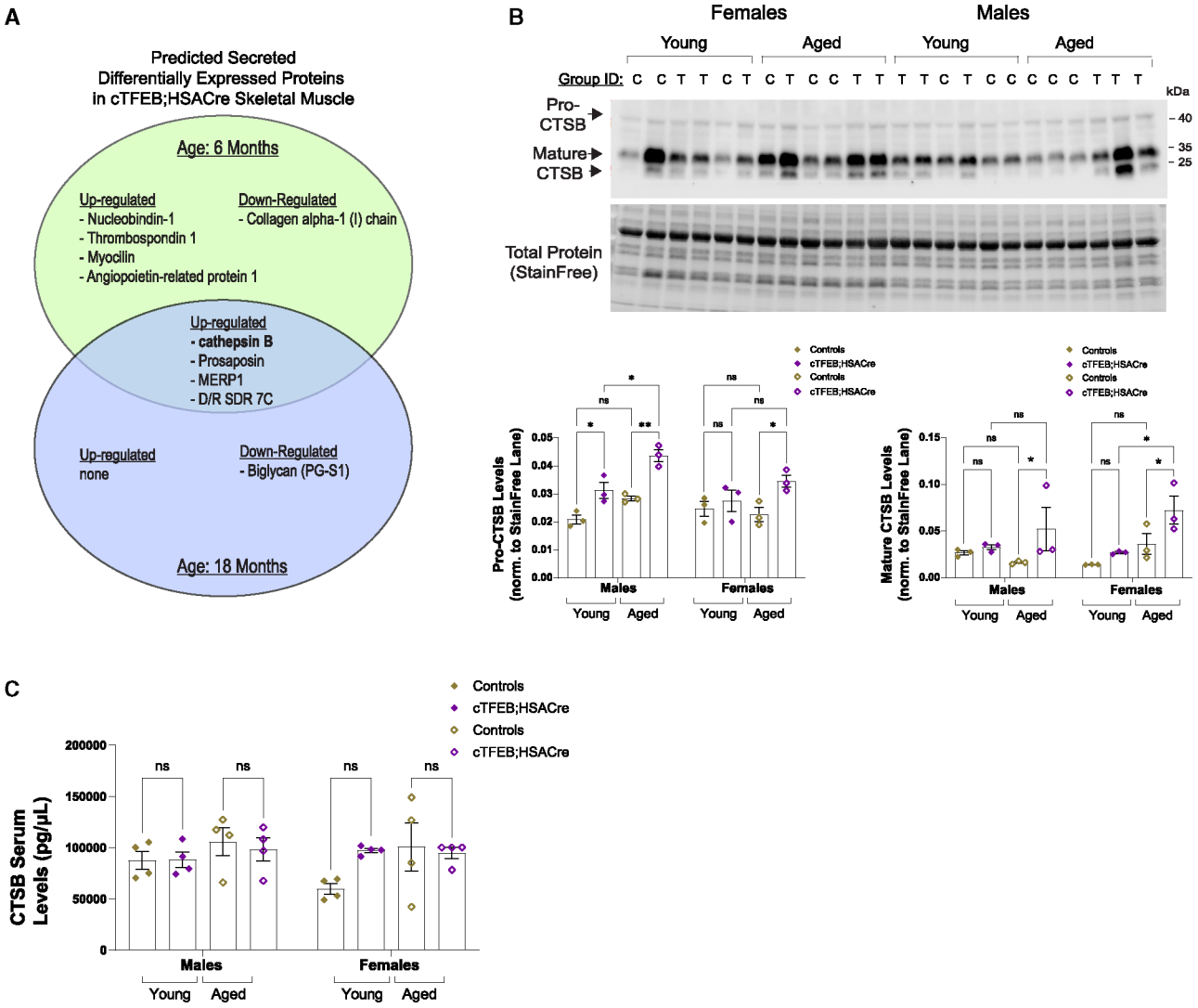

Figure 3. Increased levels of known CNS-targeting myokines in TFEB-expressing skeletal muscle

(A) Vertebrate Secretome Database (VerSeDa)-predicted secreted proteins identified as upregulated or downregulated in young (green) and aged (blue) cTFEB;HSACre muscle, from Figures 2A and 2B.

(B) Immunoblot for cathepsin B in quadriceps protein lysates from young (5–6 months) and aged (22–24 months) cTFEB;HSACre and controls of both sexes. Total protein stain-free lanes are shown as a loading control, quantification relative to protein stain-free densitometry (below).

(C) Levels of cathepsin B in serum from young (5–6 months) and aged (22–24 months) control and cTFEB;HSACre mice of both sexes. Each point represents the average of technical replicates from an individual. Controls are age-matched littermates. All data were analyzed by two-way between-subject (age × genotype) ANOVA with post hoc multiple comparisons, data are presented as mean ± SEM. *$p < 0.05$, **$p < 0.01$. Lack of annotation indicates that comparisons were not significant.

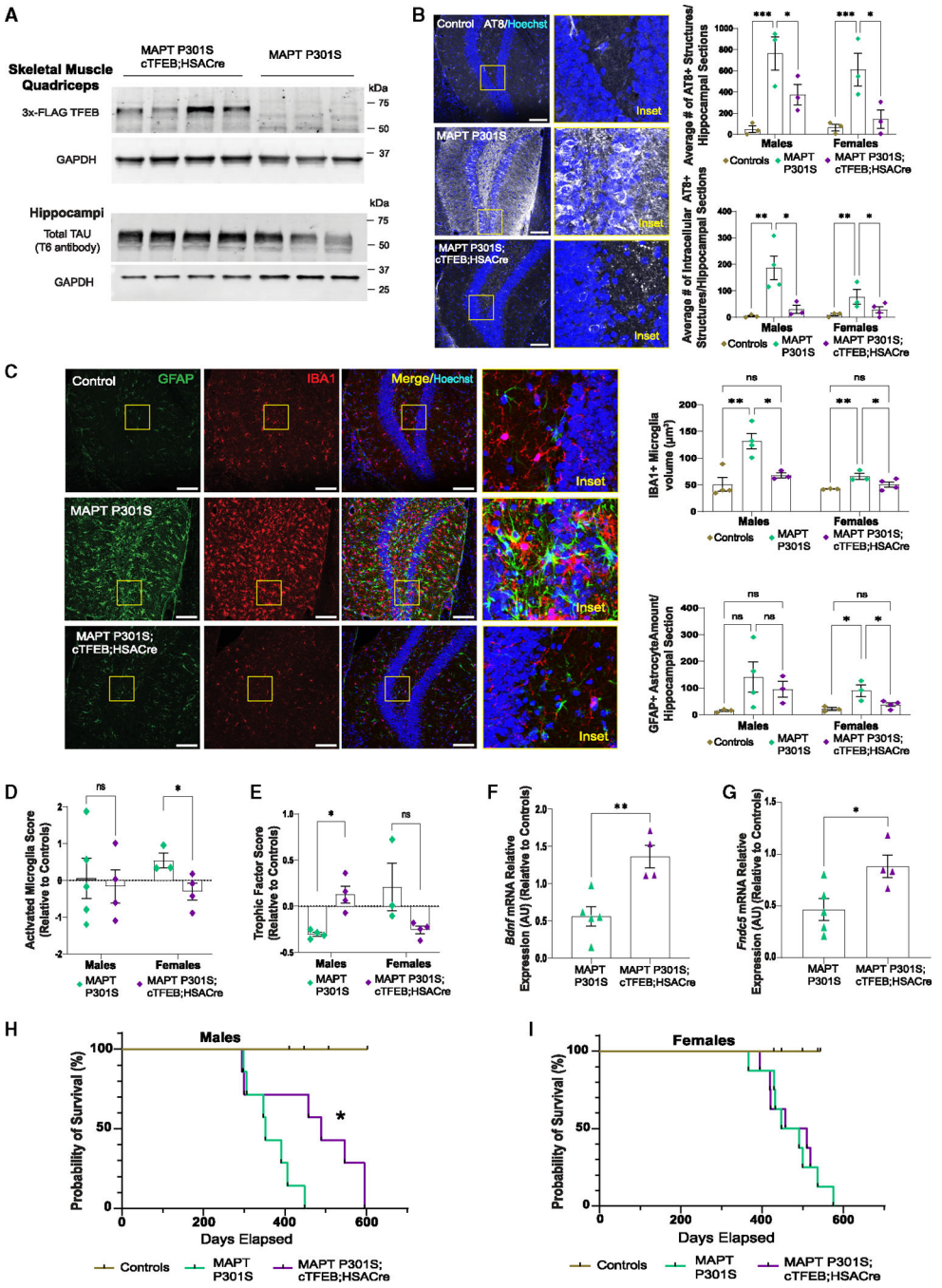

Figure 4. Skeletal muscle TFEB overexpression reduces accumulation of hyperphosphorylated tau and microglial activation in a mouse model of tau pathology

(A) Immunoblot of 3x-FLAG TFEB protein in quadriceps muscle lysates from 9-month-old MAPT P301S;cTFEB;HSACre and MAPT P301S mice (top). Immunoblot for total tau protein (T6 antibody) in hippocampal lysates from same individuals (bottom). GAPDH is shown below as a loading control.

(B) Representative merged images of the hippocampus dentate gyrus stained for phosphorylated tau (AT8, white) and nuclei/Hoechst (blue) in 9-month-old control (top, in gold), MAPT P301S (middle, in teal), and MAPT P301S;cTFEB;HSACre mice (bottom, in

purple). Quantification of total phosphotau staining/section (right, top) and for intracellular phosphotau staining (right, bottom). Scale bars, 100 μm.

(C) Representative merged images of the dentate gyrus stained for astrocytes (GFAP, green), microglia (IBA1, red) and nuclei (Hoechst, blue) in same groups as above. Quantification of IBA1+ microglia volume (top, right) and GFAP+ astrocyte staining amounts per section (bottom, right). Insets are 5× zooms of areas demarcated by yellow squares. Representative images are from male mice. Each point represents the average of all sections containing the dentate gyrus (two to three sections) for an individual animal. Scale bars, 100 μm.

(D and E) NanoString nCounter AD panel of differentially expressed gene clusters associated with microglial activation (D) or with trophic factors (E) in P301S MAPT hippocampi (teal) compared with MAPT P301S;cTFEB;HSACre (purple) age-matched littermates of both sexes relative to controls. Analysis done via nSolver (NanoString) differential gene expression analysis software. Each point represents cluster scoring for a single individual hippocampal mRNA lysate.

(F and G) qRT-PCR for *Bdnf* (F) and *Fndc5* (G) expression in hippocampal RNA lysates from 9-month-old male MAPT P301S (teal) and MAPT P301S;cTFEB;HSACre mice (purple) relative to controls.

(H and I) Survival curves for male (H) and female (I) control (gold), MAPT P301S (teal), and MAPT P301S;cTFEB;HSACre mice (purple). Controls are littermates. Unless otherwise noted, data are represented as mean ± SEM. *$p < 0.05$, **$p < 0.01$, ***$p < 0.001$, one-way ANOVA, post hoc multiple comparisons (B and C), t test (D and G), and log rank (Mantel-Cox) test (H and I). Lack of annotation indicates comparisons were not significant.

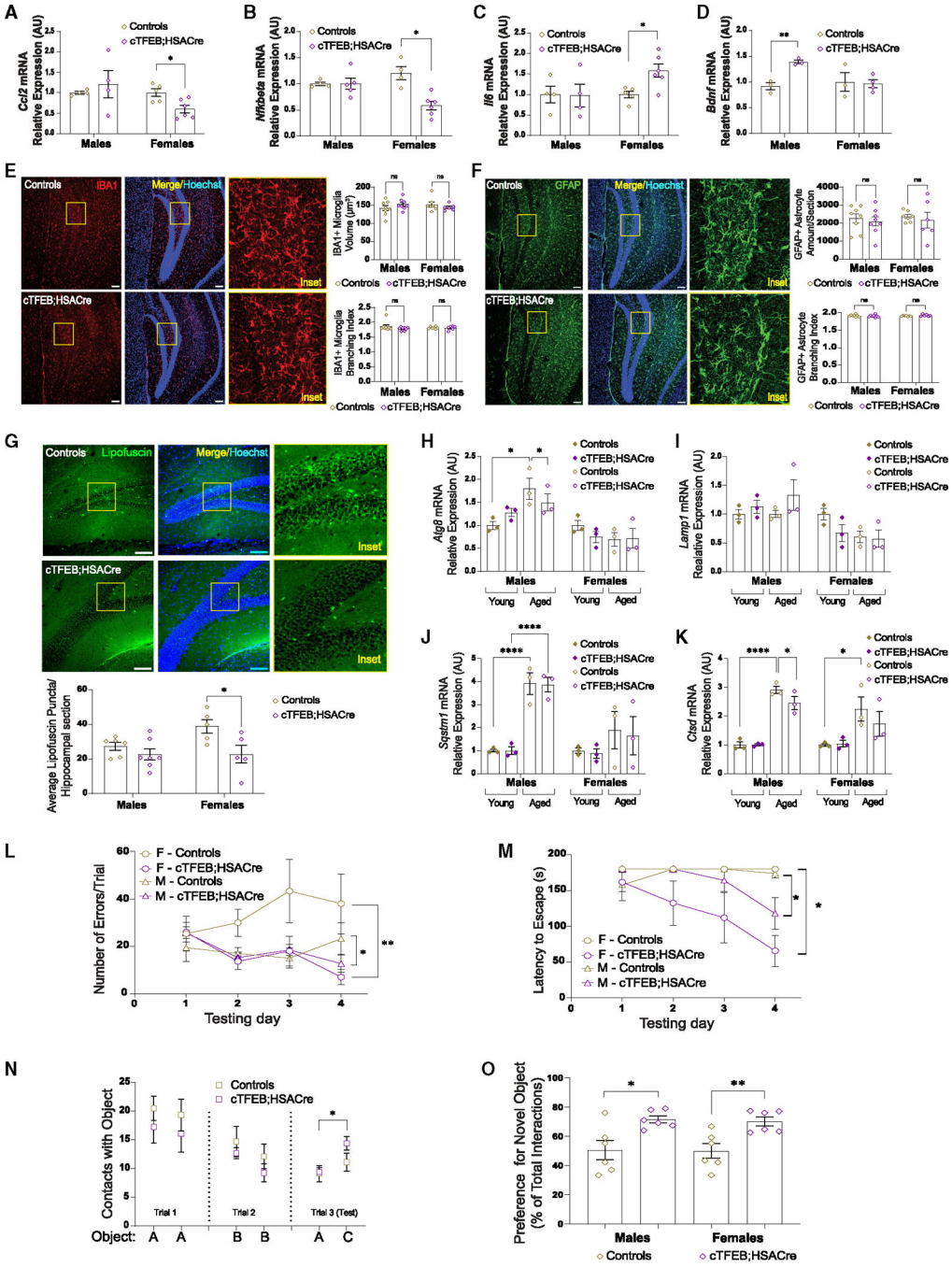

Figure 5. Skeletal muscle TFEB overexpression decreases neuroinflammation and lipofuscin accumulation and improves cognitive performance in aged mice

(A–D) qRT-PCR for *Ccl2* (A), *Nfkb* (B), *Il6* (C), and *Bdnf* (D) expression in hippocampal mRNA lysates from 18-month-old cTFEB;HSACre mice and controls.

(E and F) Representative images of the dentate gyrus of the hippocampus stained for Hoechst (blue), IBA1 (E) (red, representative images are from females), and GFAP (F) (green, representative images are from males) in 18- to 22-month-old control (top) and cTFEB;HSACre (bottom) mice. Scale bars, 100 μm.

(G) Representative merged images of the same animals as above stained for Hoechst (blue), and lipofuscin puncta (autofluorescence, green, representative images are from females). Insets depicting glia morphology are 5× zooms of areas demarcated by yellow squares. Each point represents the average of all sections containing the dentate gyrus from an individual. Scale bars, 100 μm.

(H−K) qRT-PCR for *Atg8* (H), *Lamp1* (I), *Sqstm1* (J), and *Ctsd* (K) expression in hippocampal lysates from young (6 months old, closed diamonds) and aged (21 months old, open diamonds) cTFEB;HSACre mice (purple) and controls (gold).

(L−O) Neurocognitive phenotyping of aged (18 months old) cTFEB;HSACre and control animals. Barnes maze (L and M), novel object recognition (N and O). Controls are age-matched littermates. Each point represents the average of all data collected from an individual. Data are represented as mean ± SEM. *$p < 0.05$, **$p < 0.01$, one-way ANOVA or two-way RMANOVA, post hoc tests. Lack of annotation indicates comparisons were not significant.

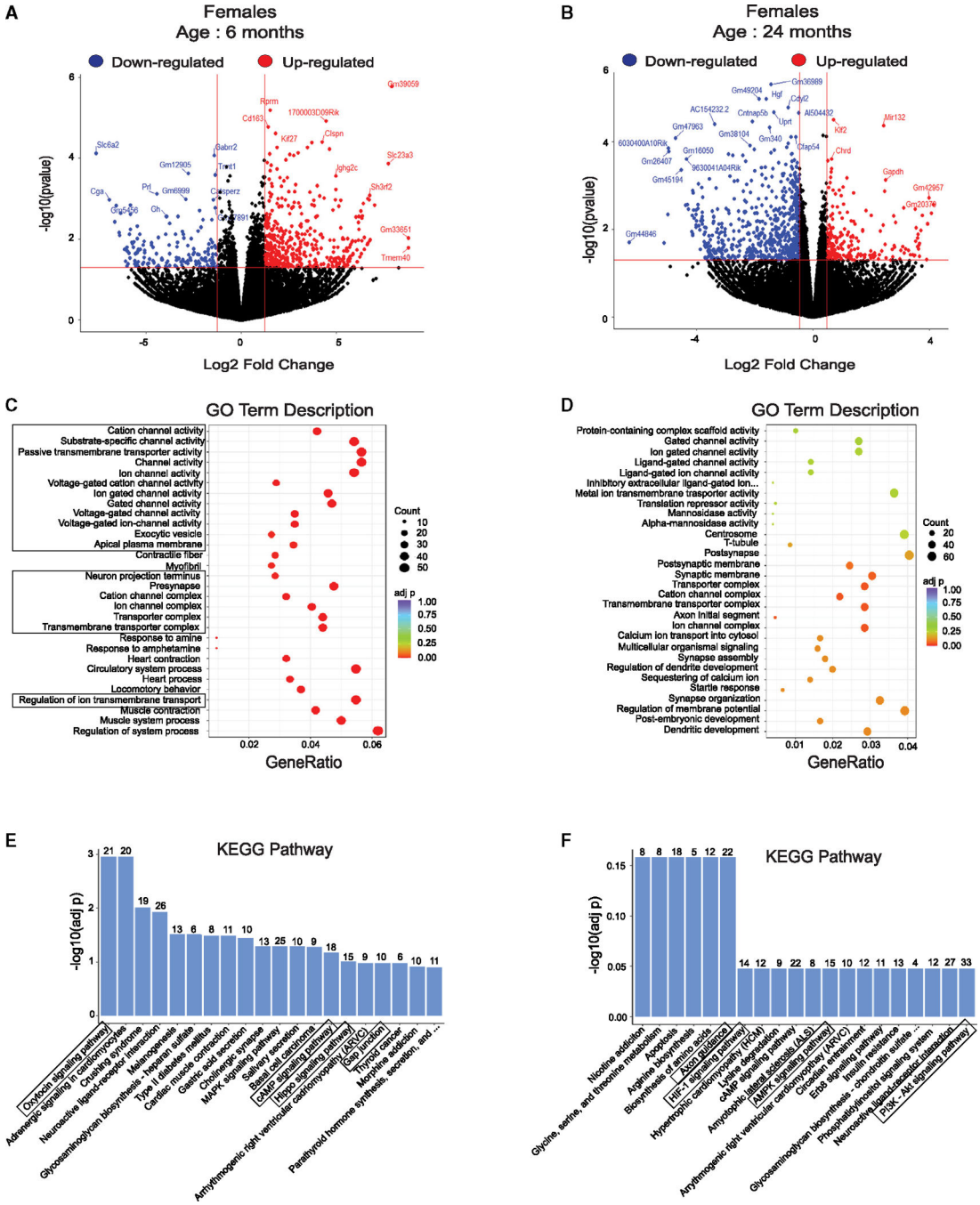

Figure 6. Transcriptome changes in the hippocampi of female cTFEB;HSACre transgenic mice suggest synaptic remodeling and improved synaptic function

(A and B) Volcano plot of differentially expressed genes in hippocampal lysates from female young (A) (6 months old) and aged (B) (24 months old) cTFEB;HSACre mice relative to controls.

(C and D) GO term analysis of differentially expressed genes from (A and B) including gene counts and adjusted p values. Boxes highlight neurotrophic signaling pathways.

(E and F) KEGG analysis of differentially expressed genes from (A and B). Number of differentially expressed (DE) genes are shown above each category. Boxes highlight categories associated with neural function.

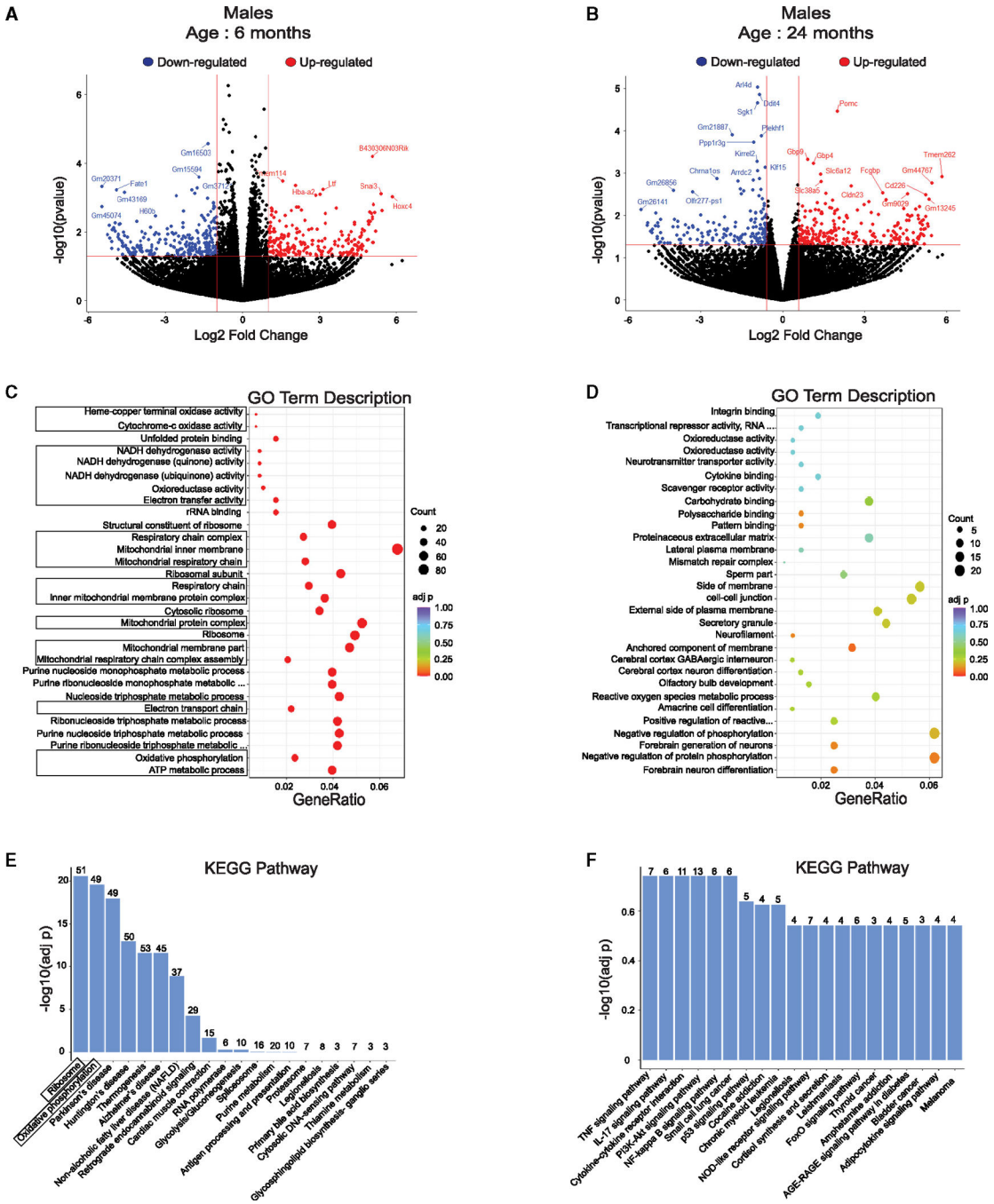

Figure 7. Transcriptome changes in the hippocampi of male cTFEB;HSACre transgenic mice suggest activation of mitochondrial and ribosomal signaling

(A and B) Volcano plot of differentially expressed genes in hippocampal lysates from male young (A) (6 months old, 2-fold change) and aged (B) (24 months old, 1.25-fold change) cTFEB;HSACre mice relative to controls.

(C and D) GO term analysis of differentially expressed genes from (A and B) including gene counts and adjusted p values. Boxes highlight ribosomal and mitochondrial pathways.

(E and F) KEGG analysis of differentially expressed genes from (A and B). Number of differentially expressed (DE) genes are shown above each category. Boxes highlight ribosomal and mitochondrial pathways.

KEY RESOURCES TABLE

REAGENT or RESOURCE	SOURCE	IDENTIFIER
Antibodies		
Mouse monoclonal anti-FLAG® M2	Sigma-Aldrich	RRID: AB_262044
Rabbit anti-TFEB	Cell Signaling Technology	RRID: AB_11220225
Rabbit monoclonal anti-LC3A/B	Cell Signaling Technology	RRID: AB_2617131
Mouse IgG1 monoclonal anti-GAPDH	Invitrogen	Cat #: AM4300
Rat IgG2a monoclonal anti-LAMP1	DSHB	Cat#: 1D4B; RRID:AB_2134500
Rabbit anti-SQSTM1/p62	Cell Signaling Technology	Cat#: 5114T
Mouse monoclonal anti-Ubiquitin	Santa Cruz Biotechnology	RRID: AB_628423
Rabbit polyclonal anti-Cathepsin B (H190)	Cell Signaling Technology	RRID: AB_2292384
Goat polyclonal anti-Cathepsin D (C-20)	Santa Cruz	RRID: AB_637896
Chicken polyclonal anti-GFAP	Abcam	RRID: AB_304558
Rabbit polyclonal anti-IBA1	FUJIFILM Wako Shibayagi	RRID: AB_839504
Mouse monoclonal anti-Phospho-Tau (Thr231) (AT180)	Thermo Fisher Scientific	RRID: AB_223649
Mouse monoclonal anti-Phospho-Tau (Ser202, Thr205) (AT8)	Thermo Fisher Scientific	RRID: AB_223647
Rabbit polyclonal anti-Laminin	Abcam	RRID: AB_298179
Rabbit polyclonal anti-LC3B	Cell Signaling Technology	RRID: AB_915950
Guinea Pig polyclonal anti-p62	Progen	RRID: AB_2687531
Mouse monoclonal anti-Myosin Heavy Chain Type I	DSHB	RRID: AB_2235587
Mouse monoclonal anti-Myosin Heavy Chain Type IIA	DSHB	RRID: AB_2147165
Mouse monoclonal anti-Myosin Heavy Chain Type IIB	DSHB	RRID: AB_2266724
Bacterial and virus strains		
pCMV-human TFEB (NM_007162) Human Untagged Clone	Origene	CAT#: SC122773
Chemicals, peptides, and recombinant proteins		
2,2,2-Tribromoethanol ≥99%	VWR	Cat#: BT145585
2-Methyl-2-butanol 99%	VWR	Cat#: TS16662–0010
TRIzol	Invitrogen	Cat#: 15596026
Turbo DNase	Thermo Fisher	Cat #: AM2238
Sybrgreen	Life Technologies	Cat#: 4309155
RIPA Lysis and Extraction Buffer	Invitrogen	Cat #: 89900
1X Halt™ Protease and Phosphatase Inhibitor Cocktail	Invitrogen	Cat #: 78442
iScript™ cDNA Synthesis Kit	BioRad	Cat #: 1708891
SYBR™ Green PCR Master Mix	Life Technologies	Cat#: 4309155
Critical commercial assays		
Pierce™ BCA Protein Assay Kits	Invitrogen	Cat #: 23225
Mouse Cathepsin B ELISA Kit	Abcam	Cat #: ab303743

REAGENT or RESOURCE	SOURCE	IDENTIFIER
Deposited data		
TFEB Muscle proteomics	Panorama Public	ID:PXD045241
Hippocampal Bulk RNA-seq data	GEO	GEO: GSE242363
Experimental models: Organisms/strains		
Mouse: fxSTOP-TFEB	This paper	N/A
Mouse: HSA-Cre (FVB.Cg-Tg(ACTA1-cre)79Jme/J)	JAX Judith Melki	RRID: IMSR_JAX:006139
Mouse: TdTomato (B6.Cg-Gt(ROSA)26Sortm9 (CAG-tdTomato)Hze/J	JAX Philippe Soriano	RRID: IMSR_JAX:007909
Mouse: MAPT P301S (B6; C3-Tg(Prnp-MAPT*P301S)PS19Vle/J)	JAX Virginia Lee	RRID: IMSR_JAX:008169
Oligonucleotides		
Actb	IDT	Mm.PT.39a.22214843.g
Lampl	Biorad	10025636
Atg5	IDT	Mm.PT.58.29236732
CTSD	IDT	Mm.PT.58.7639164
CTSB	IDT	237299388
Fndc5	IDT	Mm.PT.58.31333197
BDNF	IDT	Mm.PT.58.28814650
Ccl2	IDT	287573375
NFkBI	IDT	287573349
IL6	IDT	Mm.pt.58.10005566
Atg8 -LC3/Map1lc3b		Mm.PT.58.29764292
Sqstml	IDT	Mm.PT.58.5854953
Human TFEB	IDT	Hs.PT.58.50432039
Oprd1	IDT	Mm.PT.58.41742748
CCL3/MIP-1alpha	IDT	Mm.PT.58.29283216
Hgf	IDT	Mm.PT.58.43661644.g
Gpr88	IDT	Mm.PT.58.43661644.g
Stap1	IDT	Mm.PT.58.31635149
Gabrr2	IDT	Mm.PT.58.6928777
Pomc	IDT	Mm.PT.58.5917321
Fosb	IDT	Mm.PT.58.10990878
S100a8	IDT	Mm.PT.58.44003402.gs
S100a9	IDT	Mm.PT.58.41787562
Gnb3	IDT	Mm.PT.58.33035404
Tlr8	IDT	Mm.PT.58.16021150
Romo1	IDT	Mm.PT.56a.11138846
Software and algorithms		
FIJI	Schindelin et al.[69]	https://imagej.net/software/fiji/
QuantStudio 3	Applied Biosystems	RRID:SCR_018712
STRING Version 12.0	STRING Consortium	RRID: SCR_005223

REAGENT or RESOURCE	SOURCE	IDENTIFIER
NanoString nCounter Analysis System	NanoString	RRID:SCR_021712